

STRUCTURAL AND FUNCTIONAL CHANGES OF CIPN
PATIENTS

STRUCTURAL AND FUNCTIONAL CHANGES IN THE
CENTRAL NERVOUS SYSTEM FOLLOWING CANCER
THERAPY

By
OI LEI WONG, M.Sc.

A Thesis
Submitted to the School of Graduate Studies
in Partial Fulfilment of the Requirements
for the Degree
Master of Science

McMaster University

©Copyright by Oi Lei Wong, August 2009

MASTER OF SCIENCE (2009)
(Medical Physics and Applied Radiation Sciences)

McMaster University
Hamilton, Ontario

TITLE: Structural and functional changes in the central nervous system
following cancer therapy

AUTHOR: Oi Lei Wong, M.Sc.(Hong Kong University of Science and Tech-
nology)

SUPERVISOR: Michael D. Noseworthy, Ph.D.

NUMBER OF PAGES: xxii, 110

Abstract

Chemotherapy Induced Peripheral Neuropathy (CIPN) is known to impact negatively on patients' quality of life. It has been reported that these patients tend to have sensitivity thresholds to stimuli, such as pain and temperature, that are different from those of normal subjects. The effect of chemotherapeutic agents on the central nervous system (CNS) has been observed; however, most of the mechanisms involved are not exactly understood. A quantitative investigation into the temperature sensitivity changes in the spinal cords and brains of chemotherapy patients would provide important information in understanding the side effects of this treatment modality. In the first part of the project, the temperature perceptual changes in terms of brain activation patterns of the chemotherapy patients with CIPN are studied using brain function MRI. In the second part of the project, the structural changes of the brain and spinal cord of chemotherapy patients with CIPN are studied using diffusion tensor imaging (DTI). High b-value ($b = 1500 \text{ s/mm}^2$) and low b-value ($b=650 \text{ s/mm}^2$) settings will be use during the spinal cord DTI scans.

Due to the sample size limitation, no comparison between healthy volunteers and CIPN patients can be done based on the existing temperature fMRI data. However, the developed temperature fMRI protocol shows good reliability in detecting temperature response. Based on the spinal cord DTI result using $b = 1500 \text{ s/mm}^2$, decrease in FA value has been observed. The corresponding FA values of CIPN patient and healthy volunteers are 0.28 ± 0.10 and 0.41 ± 0.02 , respectively. ($t\text{-test} = 2.63 > 2.447$, $p=0.05$ level of signifi-

cant) However, no significant difference is observed in other diffusion parameters. This results also suggests that application of high b-value setting is more suitable as it is better at detecting diffusion at microstructure.

Acknowledgements

It has been a pleasure to work with my supervisor, Dr. Michael Noseworthy, and other committee members, Dr. Raimond Wong and Dr. Geoff Hall. They have been very supportive and understanding toward my graduate work. I want to thank them for providing their experience and knowledge on MRI principles, research techniques, anatomical and clinical information. I also owe special thanks to Dr. Jeff Fortuna for all his advice, especially all the statistics and Matlab support. My research protocol would not be completed without their kind and generous help. Special thanks should also be given to all the MR technologists and members of the image research centre for their help and support during my M.Sc degree.

Last but not least, I want to give thanks to my family members and my fiance. They have suffered from my wake up calls in the middle of the night, and my thesis would not have been completed without their mental support as well as their continuous supply of snacks.

I want to acknowledge my employer in the Hong Kong Sanatorium and Hospital for generous financial support and for this remarkable opportunity to expand my knowledge. My two years in the Master's program have been by far the best academic experience that I have ever had. I have learned a lot, not only in knowledge from books and papers, but also in research techniques and methodologies in critical thinking.

Table of Contents

Abstract	iii
Acknowledgements	v
List of Figures	ix
List of Tables	xix
List of Notations and Abbreviations	xxi
Chapter 1 The Nervous System	1
1.1 Anatomy of the brain	2
1.2 Physiology of the brain	5
1.3 Anatomy of the spinal cord	7
1.4 Temperature sensation	8
Chapter 2 Chemotherapy Induced Peripheral Neuropathy	11
Chapter 3 Basic Principles of MRI	18
Chapter 4 BOLD MRI	27
4.1 Principles of BOLD MRI	27
Chapter 5 SEEP MRI	34
5.1 Principles of SEEP MRI	34

Chapter 6	Diffusion Tensor Imaging (DTI)	39
6.1	Principles of DTI	39
Chapter 7	Statement of the Problem and Hypotheses	46
7.1	Current Issues	46
7.2	Hypothesis	48
Chapter 8	Method Development	50
8.1	Spinal cord fMRI	50
8.2	Brain fMRI using Ramped Stimulus	56
8.3	Brain fMRI using Blocked stimulus	59
8.3.1	Block design comparison (2mins ON 2mins OFF vs 30s ON 30s OFF)	59
8.3.2	non-noxious temperature stimulation	61
Chapter 9	Materials and Methods	70
9.1	DTI in the brain and spinal cord	70
9.1.1	Data Acquisition	70
9.1.2	Data Analysis	71
9.2	fMRI in the brain	73
9.2.1	Temperature stimulation systems	73
9.2.2	Data Acquisition	75

9.2.3 Data Analysis	76
9.3 Subject Selection	77
Chapter 10 Results and Discussion	78
10.1 DTI in the brain and spinal cord	78
10.2 fMRI in the brain	93
Chapter 11 Conclusion and Future directions	100

List of Figures

3.1	Hydrogen spins align with the external magnetic field (B_0 field) with two orientations: parallel and anti-parallel. Classically, the direction of the B_0 field is set to be the same as the z-direction.	20
3.2	Charged nuclei align to and precess around the external magnetic field (B_0 field).	21
3.3	The signal intensity ($M_z(t)$) as a function of time curves. T1 recovery curves are denoted in dotted line and T2 decay curves are denoted in solid lines. At an optimal reading time (TE), the signal intensity difference between tissue samples can be enhanced. This figure demonstrates the contrast optimization using T1 recovery curves and T2 decay curves of water and fat.	23
3.4	Timing diagram of GRE sequence, where a corresponds to the 90° excitation pulse, b corresponds to slice selection gradient, c corresponds to phase encoding gradient, d corresponds to frequency encoding gradient and e corresponds to dephasing gradient for spin refocusing.	25
3.5	Timing diagram of SE sequence, where a corresponds to the 90° excitation pulse, b corresponds to 180° refocusing pulse and is applied at TE/2, c corresponds to slice selection, d corresponds to phase encoding gradient, e is necessary in refocusing the echo and f corresponds to frequency encoding gradient.	26

4.1	Oxygenated hemoglobin concentration and deoxygenated hemoglobin concentration as a function of time. Oxyhemoglobin concentration increases during the neuronal activation; however, deoxyhemoglobin concentration increases during the onset of the neuronal activation then decreases. It eventually goes back to baseline level. The whole duration of the change is around 10s.	29
4.2	Upon neuronal activation, the oxygen demand increases. This leads to the increase in the oxygen level in the blood stream at the activated area to fulfill the need. Since the blood oxygen level affects the MR signal strength, the activation area can be located by comparing the MR signal before and during the neural activation.	30
4.3	Upon neuronal activation, the oxygen demand increases. This leads to the increase in the oxygen level in the blood stream at the activated area to fulfill the need. Since the blood oxygen level affect the MR signal strength, the activation area can be located by comparing the MR signal before and during the neural activation.	30
5.1	The BOLD signal as a function of TE. The dotted line corresponds to the observed non-linear function. The solid line corresponds to the linear function predicted. The non-zero intercept is observed with the non linear function.	36

6.1	The gradient pulse pair consists of a dephasing gradient and a rephasing gradient. The rephasing gradient undoes the effect of the dephasing gradient. In the case of no diffusion (case 1), no change in the spin should be observed before experiencing the rephasing gradient. For simplicity, let's assume diffusion process being a 1D problem where the first row of the spins moved to the right. The rephasing gradient thus fails to realign all the spins. The signal in case 1 is then stronger than that in case 2.	40
8.1	Non-noxious stimulation(brushing) timing diagram that is used for Spinal cord fMRI with SEEP technique	51
8.2	The sagittal image of the same subject at different slice. The resulting activation pattern was thresholded using uncorrelated voxel method with threshold set at p=0.01. No significant activation is observed inside the spinal cord using SEEP sequence. Some activations are observed inside the spinal cord as well as in the muscle outside the spinal cord.	52
8.3	The timing diagram used for the noxious stimulation (ice pack). It is expected that a stronger BOLD signal can be generated.	53

8.4	Axial images of the spinal fMRI using EPI sequence. Figure A and B corresponds to the non-noxious stimulation (brushing on the right palm). The anatomical image is placed by the z-score map in figure A and the same z-score map is placed on top of the raw EPI image in figure D. Figure C and D corresponds to the noxious stimulation (placing an ice-pack on the right palm).The z-score map is placed on top of the anatomical image in figure C and the same z-score map is placed on top of the raw EPI image in figure D. In both cases (brushing on right palm or placing ice-pack on right palm), activation patterns outside the spinal cord were observed.	55
8.5	Schematic of the temperature stimulating system that produces ramping stimulation. By controlling the inflow and the outflow switch, the hot/cold water flows to the patient and leads to increase/decrease in temperature	57
8.6	Sample temperature measurement during the experiment	58
8.7	The time course of BOLD signal of the voxel with the best fit to the predefined ideal wavefront. Block paradigm (top time course) or real time measurement (bottom time course) were used as the hemodynamic response function during the GLM calculation. The blue, green and red lines correspond to actual the full model fit, cope partial model fit and the actual data, respectively. Neither the block paradigm or the real time measurement generate reasonable BOLD signal fit.	59

8.8	Noxious stimulation(fixed 50°C) timing diagram that is used for spinal cord fMRI with EPI technique. Two sets of fMRI scan were done.(30s rest and 30s temperature stimulus cycle and 2 minutes rest and 2 minutes temperature stimulus cycle.) . . .	61
8.9	The time course of BOLD signal of the voxel showing the best fit to the assumed hemodynamic response function. The figure at the top corresponds to the 30s and 30s OFF stimulation over 100 time points (each time point equals to 1 TE). The figure at the bottom corresponds to the 2min ON and 2min OFF stimulation over 400 time points (each time point equals to 1 TE). The blue, green and red lines correspond to the full model fit, cope partial model fit and the actual data, respectively.	62
8.10	Experimental set up of the temperature stimulation system for block designed temperature stimulation	64
8.11	Temperature stimulus timing diagram that was used for 4 different non-noxious temperature settings. The solid line corresponds to the assumed hemodynamic response for GLM analysis and the dotted line corresponds to the actual stimulus timing. . . .	65
8.12	The F-test result from the multiple regression analysis on two healthy volunteers. (subject A: $p = 1.2 \times 10^{-3}$, $F = 4.59$. subject B: $p = 1.2 \times 10^{-3}$, $F = 4.59$) It shows that the activation at the sensory cortex (indicated using red arrow) is highly correlated across all 4 temperature settings.	66

8.13 The F-test result map of the same subject (thresholded at $p=1.2 \times 10^{-3}$, $F=4.59$) imaged on three different dates. Similar activation was observed on the sensory cortex.(indicated using red arrow) 67

8.14 The F-test result from the multiple regression analysis based on the test results was done on the same healthy volunteer on the same day. (thresholded at $F = 3.7$, $p =3.5 \times 10^{-2}$) Figure A corresponds to the test done on the palm. Figure B corresponds to the test done on the forearm. Stronger correlations in the somatosensory cortex (indicated using red arrow)were obtained in the forearm case. 69

9.1 Modified temperature stimulus timing diagram that was used for 4 different non-noxious temperature settings. Temperature stimulus was applied alternately on the right palm and the left forearm of the same patient. The solid line corresponds to the assumed hemodynamic response for GLM analysis and the dotted line corresponds to the actual stimulus timing. 75

10.1	All four figures above are obtained from the same subject at the same location. Figure A and C correspond to the masked FA map before applying the linear registration. Figure B and D correspond to the linearly transformed masked FA map. Both grey matter masks (Figure A and B) and white matter masks (Figure C and D) show improvement in localization after the application of linear transformation.	79
10.2	The plots of the mean and standard deviation (represented as the error bars) of FA, ADC and eigenvalues (λ_1 , λ_2 and λ_3) using ROI analysis (white matter (WM) and grey matter (GM) of the whole brain). The scans are done with $b = 900\text{s}/\text{mm}^2$. No difference between the healthy volunteers and the CIPN patients are observed based on the FA, ADC and eigenvalues of the white matter and grey matter obtained in this study.	82
10.3	The t-score maps (thresholded at t-score = 2.44, $p = 0.0505$) based on the VBM result. Voxel by voxel FA value comparison between the healthy volunteers and CIPN patients was done. . .	85
10.4	The t-score maps (thresholded at t-score = 2.44, $p = 0.0505$) based on the VBM result. Voxel by voxel ADC value comparison between the healthy volunteers and CIPN patients was done. .	86
10.5	The t-score maps (thresholded at t-score = 2.44, $p = 0.0505$) based on the VBM result. Voxel by voxel λ_1 value comparison between the healthy volunteers and CIPN patients was done.	86

10.6	The t-score maps (thresholded at t-score = 2.44, p = 0.0505) based on the VBM result. Voxel by voxel λ_2 value comparison between the healthy volunteers and CIPN patients was done.	87
10.7	The t-score maps (thresholded at t-score = 2.44, p = 0.0505) based on the VBM result. Voxel by voxel λ_3 value comparison between the healthy volunteers and CIPN patients was done.	87
10.8	The plots of the mean and standard deviation (represented as the error bars) of FA, ADC and eigenvalues (λ_1 , λ_2 and λ_3) using ROI analysis (the whole spinal cord). No difference between the healthy volunteers and the CIPN patients are observed base on the ADC and eigenvalues value of the white matter and grey matter obtained in this study. CIPN patients seem to have a smaller FA value based on the b=1500s/mm ² case.	91
10.9	The F-map (thresholded at F = 2.757, p =0.051) from the ANOVA test based on the result from 5 healthy volunteers. No significant difference between temperature settings is observed. (F-map < 5.41, 0.05 significant level)	95

10.10 Analysis result from the hypersensitive CIPN patient. Figures A to D are the correlation coefficient maps of the same slice (threshold setting: $t=1.98$, $p = 0.0509$) for 12°C , 21°C , 35°C and 40°C , respectively. Activation on the left and right sensory cortex are observed for all temperature settings. Figure E is the F-test map from the multiple regression analysis (threshold setting: $F=5$ $p=6.2 \times 10^{-4}$) 96

10.11 Analysis result from the hyposensitive CIPN patient. Figures A to D are the correlation coefficient maps of the same slice (threshold setting: $t=1.98$, $p = 0.0509$) for 12°C , 21°C , 35°C and 40°C , respectively. Activation on the left and right sensory cortex are observed for all temperature settings. Figure E is the F-test map from the multiple regression analysis (threshold setting: $F=5$ $p=6.2 \times 10^{-4}$) 97

10.12 Analysis result from a healthy subject. Figures A to D are the correlation coefficient maps of the same slice (threshold setting: $t=1.98$, $p = 0.0509$) for 12°C , 21°C , 35°C and 40°C , respectively. Activation on the left and right sensory cortex are observed for all temperature settings. Figure E is the F-test map from the multiple regression analysis (threshold setting: $F=5$ $p=6.2 \times 10^{-4}$) 98

List of Notations and Abbreviations

AFNI	Analysis of Functional NeuroImages
AIR	Automatic Image Registration
BOLD	Blood oxygen level dependent
CT	Computed Tomography
CV	Control Variable
DeoxyHB	Deoxyhemoglobin
DTI	Diffusion Tensor Imaging
EPI	Echo planar imaging
FEAT	FMRI Expert Analysis Tool
FLIRT	FMRIB's Linear Image Registration Tool
FNIRT	FMRIB's Non-linear Image Registration Tool
BET	Brain Extraction Analysis Tool
fMRI	Functional Magnetic Resonance Imaging
FSL	FMRIB's Software Library
GE	General Electric
GRE	Gradient recalled echo
IT	Inversion Time
MRI	Magnetic resonance imaging
MR	Magnetic resonance
MRI	Magnetic resonance imaging
OxyHB	Oxyhemoglobin

PCA	Principle component analysis
PET	Positron Emission Tomography
ROI	Region of interest
SEEP	Signal enhancement by extravascular protons
T	Tesla
T_1	Longitudinal relaxation parameter
T_2	Transverse relaxation parameter
T_2^*	Transverse relaxation parameter (effective)
TE	Echo time
TR	Repetition time

Chapter 1

The Nervous System

The nervous system can be divided into the central nervous system (CNS) and the peripheral nervous system (PNS). The CNS includes the brain and the spinal cord while the PNS includes cranial and spinal nerves (Carpenter 1991). Both the CNS and the PNS are protected and supported by neuroglia. However, the organization of nerve tissue in CNS is different from PNS due to the presence of different type of neuroglia (Martini 2006). There are four types of neuroglia in the CNS: ependymal cells, astrocytes, oligodendrocytes and microglia. Similar types of neuroglia, satellite cells and schwann cells can be found in the PNS (Martini 2006).

The nervous system is composed of neuronal cells. The unique structures of these cells allow the transmission and processing of external and internal information. The structures of a neuron can be divided into cell body, axons and dendrites. The cell body of a neuron contains grey colored cellular structures. Areas with high population of neuronal cell bodies are referred to as the grey matter. Axons are long cytoplasmic extensions running down from the neural cell body. They allow the propagation of electric impulse during

action potential. Dendrites are heavily branched extensions from a neuron cell body. A neuron in the CNS receives information from others mainly through dendrites. Some axons and dendrites are wrapped with white myelin sheets. Areas with high population of neuronal cell bodies are referred to as the white matter.

There are four types of neurons: anaxonic neurons, bipolar neurons, unipolar neurons and multipolar neurons. Most sensory neurons in the PNS are unipolar neurons, which extend between the sensory receptors and the CNS.

1.1 Anatomy of the brain

The brain is considered to be one of the most important organs in the human body. It is a walnut-shaped body of tissue located inside the skull and surrounded by cerebrospinal fluid (CSF) (Martini 2006). The skull provides protection from external forces, while the CSF provides support and damping to minimize the movement of the brain inside the skull (Martini 2006) (Kandel et al. 2000). The CSF contains nutrients and minerals, which allow ion exchange with the brain and the spinal cord (Greger and Windhorst 1996). Generally, the brain can be divided into three subdivisions: a pair of cerebral hemispheres, the brain stem, and the cerebellum.

Separated by the longitudinal cerebral fissure, the paired cerebral hemispheres are mirrors of each other. Generally, the left cerebral hemisphere processes motor and sensory signals from the right side of the body, while the right hemisphere processes signals from the left body side (Martini 2006). The cerebral hemispheres are composed of grey cortex (neural cell bodies) on top of the white matter, basal ganglia and subcortical neuronal masses. Each cerebral hemisphere can be divided into 6 lobes: frontal, temporal, parietal, occipital, insular, and limbic lobe (Kandel et al. 2000). The brain stem is partially embedded under the cerebral hemispheres and the cerebellum. It can be divided into the medulla, the pons and the midbrain (Barker et al. 2003). The brain stem plays an important role in controlling respiration, consciousness and functions of the cardiovascular system. More importantly, it contains some of the origins of the ascending and descending pathways linking the spinal cord to supraspinal structures (Martini 2006) (Barker et al. 2003).

Although the brain makes-up only 2% of a human's body weight, it consumes about 46mL of oxygen per minute on average (Martini 2006). This consumption requires a blood flow of approximately 750 -1000 mL per minute (Kandel et al. 2000). While the CSF does provide nutrients to the brain, it is the complex network of blood vessels embedded in the brain that provides the necessary supplements during heavy metabolic activities. In fact,

any interference in the cerebral circulation can cause necrosis and may lead to neurological or mental disturbances (Martini 2006). Depending on the location of the necrotic tissue, such lesions may also cause sensory and motor deficits (Kandel et al. 2000). Since the brain is such a delicate and yet important organ, the chemicals going into the interstitial fluid of the CNS are well regulated by the blood-brain barrier (BBB) (Greger and Windhorst 1996). The presence of the BBB not only blocks the entry of toxins and bacteria, it also prevents any chemicals, such as hormones, from altering neuronal activity (Martini 2006). The BBB is a layer of tightly-packed ependymal cells surrounding the brain's blood vessels, which are then surrounded by astrocyte cells to provide biochemical support (Martini 2006). The presence of the BBB mostly allows small hydrophobic molecules to pass and blocks away hydrophilic ones (Greger and Windhorst 1996). As for larger molecules such as glucose, there exist active transport channels to allow specific molecular exchange between the blood and the brain. The reduction of the astrocyte cells results in the loosening of the BBB (Martini 2006). It is also worth noting that several areas of the brain may lack the BBB, such as some portions of the hypothalamus, the posterior lobe of the pituitary gland, the choroid plexus and the pineal gland (Greger and Windhorst 1996). Generally, structures similar to the BBB may also be found along the spinal cord and optic nerves.

1.2 Physiology of the brain

The CNS is responsible for high-order neurofunctions. Besides processing neurological stimuli from the environment, the brain is also responsible for higher neural activities such as memory tasks, motor activity, maintaining homeostatic balance, sleep, emotion expression and learning (Guyton 1991). Since the sensory function of human subjects is investigated in this project, a brief introduction to the cognitive functions of the various brain areas is given here.

The cerebral cortex, the heavily folded structure at the surface of the cerebral hemisphere, plays an important role in cognitive functions. The cerebral cortex can be divided into various parts according to the type of stimulus. Broca's speech area is associated with motor functions involved with speech (Barker et al. 2003). The prefrontal area is responsible for behavioral functions such as personality and expression of emotion. The premotor area is associated with motor activity in response to sensory input, whereas the primary motor area is associated with voluntary motor activity. The primary somesthetic cortex processes sensory stimuli, such as temperature, while the somesthetic association area processes pain stimuli from the peripheral system. The visual cortex processes the stimulus from the eyes into simple information, such as orientation and color, while the visual association area integrates the

processed information into more complex properties such as figure recognition. Similarly, the primary auditory cortex processes the stimulus from the ear and the auditory association area processes the information into more complex properties. The sensory speech area is specialized to process speech related sensory activity and leads to speech recognition (Martini 2006).

Besides the cerebral cortex, the thalamus is also important for sensation (Guyton 1991). It has two ellipsoidal structures, one for each hemisphere, located on top of the mid-brain and under the corpus callosum (Carpenter 1991). The thalamus is involved in important tasks such as the regulation of sleeping states and consciousness. It is thought that the thalamus is also responsible for preprocessing sensory information and passing the information to the associated area of the brain (Guyton 1991). However, the mechanism is not completely understood.

Nervous cells do not regenerate and thus, physical damage to the brain is usually permanent (Martini 2006). However, the brain has high plasticity. Instead of regenerating new nervous cells, it is believed that the number of nerve fibers generated in the existing nervous cells increases. For instance, if the sensory cortex of the left brain (dominant side) is damaged, the sensory cortex of the right brain (the non-dominant side) becomes activated regardless of whether the left or right hand is stimulated. Such remapping can be

identified with recovered stroke patients or phantom limb patients (Johnston 2009) (Kandel et al. 2000).

1.3 Anatomy of the spinal cord

The spinal cord is a cylindrical structure that extends from the end of the medullary pyramid to the lower border of the first lumbar vertebra. It is located in the vertebral column and is protected by the CSF (Martini 2006). Like the brain, the spinal cord is composed of grey matter and white matter. Grey matter is a butter-fly shaped grey structure located in the middle of the cord while white matter is located in the peripheral area (Carpenter 1991). The organization of the spinal cord is such that it can be generalized into various regions according to their functions (Guyton 1991). The white matter regions in the spinal cord can be divided into the posterior white columns, the anterior white columns, the anterior white commissure and the lateral white column. The central grey matter can be classified into the following regions based on functionality: the somatic sensory region, the visceral sensory region, the somatic motor and visceral motor function areas (Barker et al. 2003).

Generally, the spinal cord may be divided into thirty-one segments: eight cervical, twelve thoracic, five lumbar, five sacral and one coccygeal. Each segment is connected to a pair of spinal nerves that exit the vertebral column

from the intervertebral foramina (Barker et al. 2003). Each spinal nerve can be further divided into dorsal and ventral root filaments, which unite at the dorsal root ganglion and emerge as a mixed spinal nerve (Barker et al. 2003). Usually, the dorsal root fibers are absent from the first cervical and coccygeal roots (Martini 2006). The nerve fibers are organized such that the ones responsible for leg and buttock sensations go into the sacral and lumbar spine, respectively (Carpenter 1991). Those responsible for chest and abdomen sensations go into the thoracic spine and those responsible for arm, neck and the back of head sensations go into the cervical spine (Barker et al. 2003). In fact, each spinal nerve is responsible for monitoring a specific part of the skin's surface (Martini 2006). For example, a somatosensory stimulus is first detected by sensory receptors in the palm and then reaches the dorsal roots at C6 to the T1 spine (Martini 2006) (Guyton 1991).

1.4 Temperature sensation

The white matter contains myelinated (A-fibers and B-fibers) and unmyelinated axons (C-fibers), (Guyton 1991) which run along the vertebral column in a fairly parallel manner. It is the myelination of the axon that leads to the white appearance. Both the myelinated and unmyelinated axons form the ascending and descending spinal tracts that connect the peripheral nerves

to the brain (Martini 2006). Generally, the sensory pathways correspond to the ascending pathways from the spinal cord while the motor pathways correspond to the descending pathways of the spinal cord (Martini 2006) (Barker et al. 2003). The myelin sheath protects the electrostatic balance of the nerves. Loss of myelin sheath results in cross talking between the neighboring nerve fibers. This increases the error rate during signal transmission between the peripheral nerves and the brain.

The main function of the spinal cord is to transport signals between the brain and the receptors and to control simple reflexes. It is also believed that some signal processing is done in the spinal cord (Guyton 1991). Nerve fibers connect the receptors to the spinal cord (Barker et al. 2003). While A-fibers deliver sensory information such as position, balance, and pressure sensation, B-fibers are responsible for motor functions and C-fibers are mostly responsible for graded sensory functions, such as pain and temperature sensations (Martini 2006). Although the histology of nerve fibers and sensory receptors has been studied for decades, the mechanisms are not completely understood. For the scope of this thesis, the pathway of pain and temperature sensitivity will be discussed.

Various types of ion channels are found in sensory neurons in the PNS and respond to stimuli by transmitting molecular signals. Temperature is

thought to be related to a group of ligand-gated channels, called transient receptor potential (TRP) channels (Hwang and Oh 2007). Each type of these channels is temperature specific. For example, TRPV1 is sensitive to noxious heat temperatures ($>46^{\circ}\text{C}$), TRPV2 operates at high temperatures ($>52^{\circ}\text{C}$), TRPV4, TRPM8 and TRPA1 function at a temperatures ranging from $>30^{\circ}\text{C}$, $<25^{\circ}\text{C}$ and $<17^{\circ}\text{C}$, respectively (Hwang and Oh 2007). The graded potential amplitudes depend on the temperature level. The electric signals generated at the temperature receptors is transmitted to the ventral nucleus group of the thalamus through the lateral spinothalamic tracts (Barker et al. 2003).

Chapter 2

Chemotherapy Induced Peripheral Neuropathy

Based on the findings from Hughes et al, neuromuscular abnormalities have been detected in 2.5% to 5.5% of patients with lung or breast cancer (Custodio 2008). The cause of neuropathy may be related to the side effects of the cancer treatment such as surgery, chemotherapy, radiation therapy, hematopoietic stem cell transplantation or immunologic therapy. The severity of damage to the peripheral nervous system depends on many treatment parameters such as the location of the lesion and the level of the peripheral nervous system involved. More attention has been drawn to chemotherapy induced peripheral neuropathy (CIPN) than to the peripheral neuropathy induced by other cancer treatment methods. Also, the cause of CIPN is more complicated because of the diversity of the drugs used and other environmental factors such as the state of the patient's nutrition during the treatment.

Although almost all chemotherapeutic agents lead to side effects such as memory loss, neuropathy or cognitive change, 10 to 20% of patients are diagnosed with CIPN (Forman 1990). Such neuropathy is characterized by

dysesthesia, pain, numbness, tingling or weakness; the degree of the effect varies with the dose and the drug used. CIPN is commonly experienced at distal parts of the body such as hands, finger tips and feet. The cause of the CIPN is thought to be a result of axonal loss via Wallerian degeneration. It is part of the damaged nerve fibers repairing mechanism occurring naturally in PNS. During this process, the axon at the distal site first degenerates. The Schwann cells then proliferate to reform a solid cord so that they wrap around the axon. Finally, the axon grows along the new solid cord until the normal synaptic contacts hopefully are formed. Sometimes, the new axon path may deviate or the axon may stop growing. In this case, the damaged nerve fiber cannot be restored (Martini 2006). Since the CNS has regions with high density of nerve tissue, it is harder for the damaged part to be fully recovered.

Vinca alkaloids, taxanes and platinum based compounds are commonly used during chemotherapy treatment. Vinca alkaloids, combined with other chemotherapeutic agents, are usually used to treat solid tumors, lymphomas and leukemia. Taxanes are commonly used to treat breast and ovarian cancer. It is proposed that vinca alkaloids and taxanes may cause axonal degeneration by inhibiting anterograde transport and retrograde transport. The resultant neuropathy is length-dependent and sensory function related (Custodio 2008) (Quasthoff and Hartung 2002) (Wickham 2007).

Platinum based compounds are used to treat solid tumors such as ovarian, testicular and bladder cancer. "Coasting phenomenon" is the characteristic side effect, where the sensory dysfunction involved is caused by damage to the dorsal root ganglia (Tracey et al. 2000). The sensory functional change is more often observed in the upper extremities than the lower extremities. It is worth noting that incomplete recovery is expected in this case (Custodio 2008) (Quasthoff and Hartung 2002) (Wickham 2007).

Suramin is an experimental drug that is designated for the treatment of solid tumors such as prostate and ovarian cancer. Although the mechanism remains unclear, the cyto-toxicity and neuro-toxicity associated are thought to be the result of growth factor inhibition. It is known that suramin induces the blocking effect on P2 purinegic receptors, which are involved in the intracellular signal transduction pathways in the peripheral nervous system (PNS). Neural cell damage thus results when these pathways are blocked. Patients under high dosage of suramin may suffer from sensory-motor symptoms even though suramin is expected to affect demyelinated nerve fibers only (Quasthoff and Hartung 2002).

During chemotherapy, a combination of chemotherapeutic agents is prescribed to the patient. However, it has been observed clinically that patients suffer from unexpected neuropathy when combined chemotherapy is used. For

example, the combination of taxol and cisplatin may induce thickening of myelinated nerve fibers which is not observed when taxol or cisplatin is prescribed alone (Custodio 2008) (Quasthoff and Hartung 2002) (Wickham 2007). The side effects of most chemotherapeutic agents are known and are usually sensory function related. The potential side effects associated with the common chemotherapy drugs listed previously are listed in Table 2.1 below.

Chemo-therapeutic agent	Neurotoxic cumulative dose	Peripheral nervous system effects		Morphological changes	Other comments
		sensory	motor		
Vinca alkaloids					
Vincristine, Vinblastine	> 4mg	always	rare	Demyelination, dying back type axonal loss and dorsal root ganglia damage	1. Usually start with pain and paresthesia of feet and hands, distal dyperesthesia then loss of deep tendon reflexes. 2. Severes peripheral neuropathy may result in muscle cramps and weakness. 3. Patient with hereditary neuropathy may experience rapid onset quadriplegia, which may be partially reversible over months to years to be permanent. 4. Vincristine and vinblastine can case vocal cord paralysis, jaw pain or, in rare case, optic neuropathy due to their effect on cranial nerves. 5. Coasting can be observed.
Vinorelbine	> 4mg	rare			same as above
Taxanes					
Taxol	>175-200 mg/m ²	frequent	absent	Severe nerve fiber loss, axonal atrophy and secondary demyelination, little axonal regeneration.	1. Distal symmetrical paraesthesia pallhyparaethsia, loss of joint position sense, painful dysaesthesia and Lhermitte's signs are often reported. 2. Amplitude of sensory may be reduced according to NCS. 3. Progressive distal or proximal paresis may be observed. 3. In rare case, optic neuropathy may be observed.

Chemo-therapeutic agent	Neurotoxic cumulative dose	Peripheral nervous system effects		Morphological changes	Other comments
		sensory	motor		
Platinum Analogues					
Cisplatin	>300mg/m ²	frequent	absent	Damage of large myelinated fibers and cell bodies in dorsal root ganglia	1. Peripheral neuropathy in dose dependent. 2. Tingling at lower extremities, vibration impairment, loss of tendon reflexes, ataxia Lhermitte's sign and joint position impairment are often reported. 3. Over 75% of the patients develop neurosensor high frequency hearing loss and tinnitus. 4. Coasting is commonly observed.
Carboplatin	>400mg/m ²	less frequent	absent	Damage of large myelinated fibers and cell bodies in dorsal root ganglia	1. Peripheral neuropathy occurs after high cumulative dose and combined with other drugs. 2. Slowing of sensory response with reduced amplitude. 3. H-reflexes may be absent or prolonged. 4. Tingling at lower extremities.

Chemo-therapeutic agent	Neurotoxic cumulative dose	Peripheral nervous system effects		Morphological changes	Other comments
		sensory	motor		
Oxallplatin	>175-200mg/m ² (>14 days)	always	less frequent	unknown	1. No threshold for less than 14 days administration. 2. Early responses include dose related acute sensory symptoms shortly after administration, cold related dysesthesia and paresthesia of extremities, painful paresthesia and, although less frequently reported, shortness of breath and difficulty swallowing. 3. Persistent administration (>14 days) may lead to sensory impairment, sensory ataxia and problems with fine sensory-motor coordination. 4. Early symptoms can be resolved in a few days to two weeks. 5. Symptoms resulting from persistent drug use may be completely or partially reversible after then termination of treatment. 6. Coasting do not occur.
Others					
Suramin	>350mg (max. plasma level)	frequent	less frequent	Segmental demyelination in sural nerve biopsies	1. Dose limiting peripheral neuropathy in unmyelinated sensory and motor nerves is observed 2. Neuropathy tends to be rare. 3. Severe paresis may be observed.

Table 2.1: Summary on sensory and motor related symptoms of the chemotherapeutic agents used in this thesis. (Information of this table is obtained and modified based on Custodio C. (2008) and Quasthoff S. (2002))(Custodio 2008)(Quasthoff and Hartung 2002)

Chapter 3

Basic Principles of MRI

According to quantum mechanics, nuclei have a fixed (quantized) set of energy states that are well defined by quantum numbers. In MR physics, it is the spin quantum number that determines the maximum number of energy states. For instance, the spin quantum number (S) for hydrogen is $1/2$.(Huettel et al. 2003). Thus, the maximum allowable energy states will be (Hashemi et al. 2003)

$$\begin{aligned} \text{Maximum allowable energy states} &= 2S + 1 \\ &= 2(1/2) + 1 = 2 \end{aligned}$$

For the simplest case having a singly charged proton (the hydrogen nucleus), nuclei are spinning either parallel or anti-parallel about their axis (i.e. spinning with the magnetic dipole moment (μ) and pointing either in the same direction as the axis or in the opposite direction)(Hashemi et al. 2003) (as shown in figure 3.1). Each hydrogen nucleus spins around its axis and generates magnetic fields according to the Bloch equation. (The Bloch equation assumes

that any charged spinning particle generates a magnetic field) (Hashemi et al. 2003). Thus, any particle with unpaired protons (S is not an integer) would exhibit magnetic properties and would align with the external magnetic field (B_0 field). Any paired proton spins have the same magnitude but are opposite in direction, thus, resulting in a zero local magnetic field. Note that not all the hydrogen spins align parallel to the external magnetic field. Since nuclei naturally tend to stay in the minimum possible energy states, the majority of the spins will be in the parallel states (Taylor et al. 2004). Obviously, the magnitude of μ increases with the number of unpaired protons in the nucleus (Hashemi et al. 2003) (Buxton 2002). In fact, it is the bulk magnetization (M), which is the vector sum of the dipole moments of a group of atoms, that is of interest. Thus, the number of atoms available with unpaired protons also affects the resultant magnetization. Sodium (Na), phosphorus (P) and hydrogen (H) all have unpaired protons and are all found in the human body. Although Na has the largest spin number, S , among these elements (Hashemi et al. 2003) (Buxton 2002) (McRobbie et al. 2006), the Na content in the human body is less than that of hydrogen (a human's body is made of 0.2% sodium and 9.7% hydrogen) (Martini 2006). Na, thus, is not the most popular choice to produce MR images.

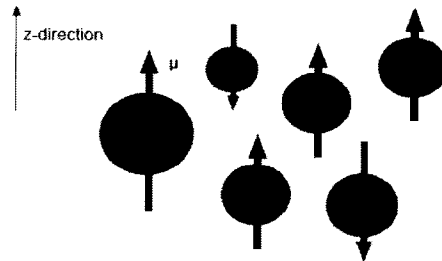


Figure 3.1: Hydrogen spins align with the external magnetic field (B_0 field) with two orientations: parallel and anti-parallel. Classically, the direction of the B_0 field is set to be the same as the z-direction.

When the hydrogen nucleus is spinning within an electromagnetic field, the nucleus starts to precess around the B_0 field at a slightly tilted angle as shown in figure 3.2. The precession follows the Larmor equation: (Hashemi et al. 2003) (Buxton 2002) (McRobbie et al. 2006) (Huettel et al. 2003)

$$\omega = \gamma B_0 \quad (3.1)$$

The Larmor equation, where : ω corresponds to the angular frequency, γ corresponds to the gyromagnetic ratio and B_0 corresponds to the external magnetic field.

It is worth noting that the gyromagnetic ratio is constant for each type of nucleus; it is independent of factors such as the B_0 field (Hashemi et al. 2003). In order to be able to produce any useful information from the nuclei, transverse and receive coils are needed. When the transverse coil

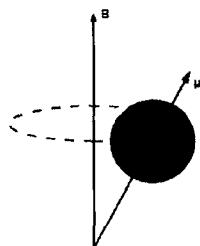


Figure 3.2: Charged nuclei align to and precess around the external magnetic field (B_0 field).

sends transverse magnetization pulses at the Larmor frequency (referred to as the excitation pulse), hydrogen nuclei start to spiral down from the minimum energy states (parallel to the B_0 field) towards the higher energy states (anti-parallel to the B_0 field) (Hashemi et al. 2003) (Buxton 2002) (McRobbie et al. 2006) (Huettel et al. 2003). Instead of tipping the hydrogen spin anti-parallel to the B_0 field, the spin is usually tipped at 90° for maximum signal detection (Hashemi et al. 2003). Since the flip angle is related to the frequency of the transverse pulse and the duration of the pulse, a flip angle of less than 90° is usually used to reduce the scanning time (Buxton 2002). The magnetic behavior of the hydrogen nuclei in the presence of a B_0 field can be described mathematically using the Bloch equation (as illustrated in equation 3.2 below) (Hashemi et al. 2003) (Buxton 2002) (McRobbie et al. 2006) (Huettel et al. 2003).

$$\frac{dB_0}{dt} = \gamma B_0 \times M \quad (3.2)$$

, where B_0 is the main magnetic field, M is the transverse magnetization and γ is the gyromagnetic ratio

The reading coil detects the changes in magnetization based on Lenz's law (Hashemi et al. 2003) and Faraday's law of induction. The induced electromagnetic force (due to the change in the magnetic flux through the current loop) is in the direction opposite to the change in flux (Taylor et al. 2004). Therefore, the electric current produced by the precessing hydrogen nuclei can be measured using a reading coil. As the hydrogen spins rotate back to align with the B_0 field after the excitation pulse, the amplitude of the measured oscillating current decreases. This measured MR signal is generally referred to as the free induction decay (FID) (Hashemi et al. 2003) (Buxton 2002). The time for the spins to realign with the B_0 field is characterized as the longitudinal relaxation time (T_1), which is also named as the spin-lattice relaxation time. The T_1 value can be dependent on the tissue type and on the strength of the B_0 field (Huettel et al. 2003). Another way to differentiate the type of tissue can be done with the T_2 relaxation time. After the excitation pulse, the signal intensity decreases due to spins dephasing transversely. In the presence of spin-spin interactions, each spin is experiencing the B_0 field

and a small magnetic field from its neighbour. Each spin then precesses with a slightly different ω . Eventually, the spins will be completely out of phase transversely at the T2 relaxation time (McRobbie et al. 2006). In reality, the spin dephasing is caused by external magnetic field inhomogeneity as well. The time for spins to be completely out of phase transversely due to spin spin interactions and the external magnetic field inhomogeneity is called the T2* relaxation time (Buxton 2002). As shown in figure 3.3 below, different signal intensities can be detected at some optimal time.

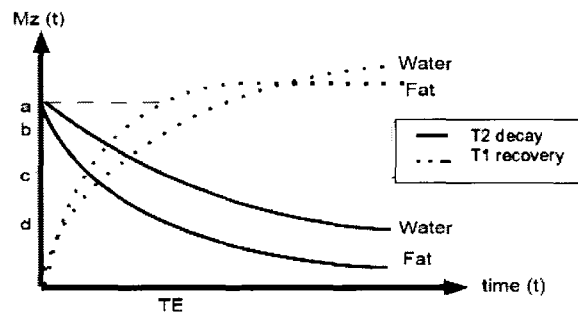


Figure 3.3: The signal intensity ($Mz(t)$) as a function of time curves. T1 recovery curves are denoted in dotted line and T2 decay curves are denoted in solid lines. At an optimal reading time (TE), the signal intensity difference between tissue samples can be enhanced. This figure demonstrates the contrast optimization using T1 recovery curves and T2 decay curves of water and fat.

Up to this point, the signals from all of the various positions in the sample are detected at the same time. Gradient slice selection, phase encoding and frequency encoding gradients are applied to allow the 2D spatial localization in the frequency domain (k-space) (Hashemi et al. 2003). During the slice

selection, the gradient field is applied perpendicular to the plane of interest so that the spins in each slice are rotating at a slightly different frequency. A slice selection sinc pulse with a centre frequency equivalent to the frequency of the slice of interest is applied (ideally, only spins with the resonance frequency equal to the centre frequency of the sinc pulse are selected) (Nishimura 1996). Another gradient field is then applied in the second dimension (G_y) for a brief period of time. The spins then precess in the $\omega + \delta\omega$ direction and are related to the positional information along k_y (Nishimura 1996). Finally, frequency encoding can be done by the application of the third gradient field (G_x). The hydrogen nuclei are then precessing with different frequencies along the k_x direction. Fourier transformation of the measured data results in the final real image (Hashemi et al. 2003).

Given that the signal is decaying during data acquisition, gradient-echo (GRE) and spin-echo (SE) are important in improving the strength of the signal. In GRE imaging, a gradient field is applied to cancel out the phase shifts and regain the spin coherence. This results in an increase in signal amplitude (Nishimura 1996) (as illustrated in figure 3.4 below).

In SE imaging, the coherence of the spins is regained using a 180° refocusing pulse (Hashemi et al. 2003). As discussed previously, spins dephase transversely after the application of the excitation pulse. In fact, this process

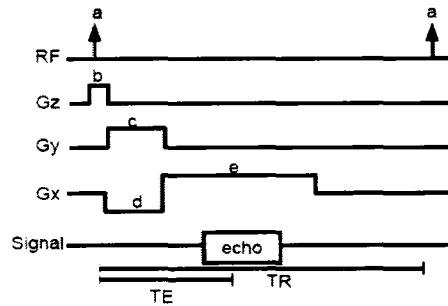


Figure 3.4: Timing diagram of GRE sequence, where a corresponds to the 90° excitation pulse, b corresponds to slice selection gradient, c corresponds to phase encoding gradient, d corresponds to frequency encoding gradient and e corresponds to dephasing gradient for spin refocusing.

is symmetric (Nishimura 1996). The application of the refocusing pulse rotates the spins without changing any other spin properties. The spins continue to precess at slightly different ω and eventually refocus (refer to figure 3.5 for timing diagram of the SE sequence). It is also worth noting that the presence of the refocusing pulse cancels out the chemical shift and field inhomogeneity effects. A T2 image, as opposed to a T2* image, can be obtained (Nishimura 1996). When compared to the GRE sequence, the SE sequence results in a shorter scan time.

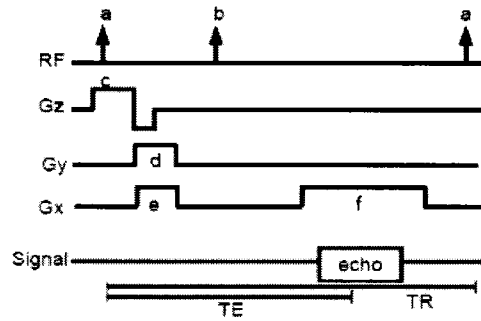


Figure 3.5: Timing diagram of SE sequence, where a corresponds to the 90° excitation pulse, b corresponds to 180° refocusing pulse and is applied at $TE/2$, c corresponds to slice selection, d corresponds to phase encoding gradient, e is necessary in refocusing the echo and f corresponds to frequency encoding gradient.

Chapter 4

BOLD MRI

4.1 Principles of BOLD MRI

Hemoglobin is a protein found mainly in red blood cells. The major role of hemoglobin is to deliver oxygen to various parts of the body. Deoxyhemoglobins are paramagnetic (μ equals to zero) due to the presence of the iron ions (Fe^{2+}), which lead to its ability to transport oxygen. When hemoglobin bind with oxygen, they are referred to as oxyhemoglobin. Those hemoglobin without binding with oxygen are referred to as deoxyhemoglobin. Oxyhemoglobin have no unpaired electrons and have zero μ (i.e. diamagnetic). (McRobbie et al. 2006). The susceptibility of oxyhemoglobin and hemoglobin are, then, different. Local magnetic gradient is created around the blood vessel in the presence of deoxyhemoglobin because of the change in magnetic susceptibility. As a result, increase in deoxyhemoglobin leads to decrease in MR signal (Huettel et al. 2003) (Ogawa et al. 1990).

The changes in the MR signal depending on the blood oxygenation level was first proposed by Ogawa in 1980s and is referred to as blood oxygen level dependency (BOLD) (Buxton 2002). It is the effect of BOLD on the $T2^*$ value that forms the basis of functional MRI. When a certain area of the brain is activated, more oxygen is consumed locally to support the neural activation. The body then responds by increasing the local oxygen level in that part of the brain. Based on the data from Malonek and Grinvald collected in 1996, the local oxyhemoglobin concentration has been observed to be higher than that of deoxyhemoglobin during neuronal activation (McRobbie et al. 2006) (refer to figure 4.1). The change in blood supply in response to the impulse stimulus is generally referred to as the hemodynamic response function.

This change results in the increase in local MR signal due to the net increase in oxyhemoglobin (McRobbie et al. 2006). There are many hypothesis regarding the hemodynamic response illustrated in figure 4.1. Buxton group, for example, explains the hemodynamic response using the balloon model (The blood vessel expands as a result of the increment of blood supply) (Feng et al. 2001). Generally speaking, it is not the activated neurons being imaged but the change in characteristic of the blood supply (Huettel et al. 2003) (mostly from the vein so as to measure the changes in oxygen level) near the activated area (refer to 4.2). The same activated area should probably be observed

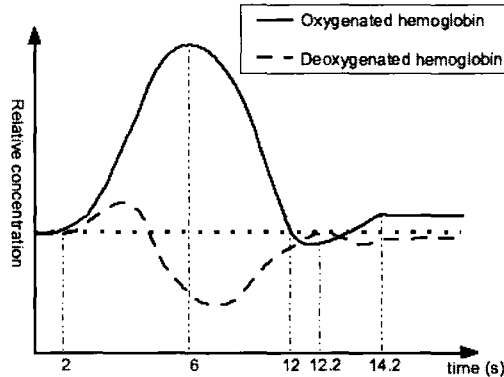


Figure 4.1: Oxygenated hemoglobin concentration and deoxygenated hemoglobin concentration as a function of time. Oxyhemoglobin concentration increases during the neuronal activation; however, deoxyhemoglobin concentration increases during the onset of the neuronal activation then decreases. It eventually goes back to baseline level. The whole duration of the change is around 10s.

with perfusion measurement (Al-Asmi et al. 2003). For the purpose of fMRI, BOLD is commonly used as it is more sensitive than perfusion measurement (McRobbie et al. 2006).

BOLD signal can be calculated using $\delta S/S$, as illustrated in figure 4.3 below (McRobbie et al. 2006). To obtain the changes in $T2^*$ value, Echo Planar Image (EPI) sequence is one of the popular choices (Huettel et al. 2003). During the fMRI acquisition, rapid scans are done continuously throughout the paradigm. For simplicity, block design paradigms, an alternation between active and rest state, are often used. Sometimes, the application of block design paradigms may not be possible. For example, patients with epilepsy

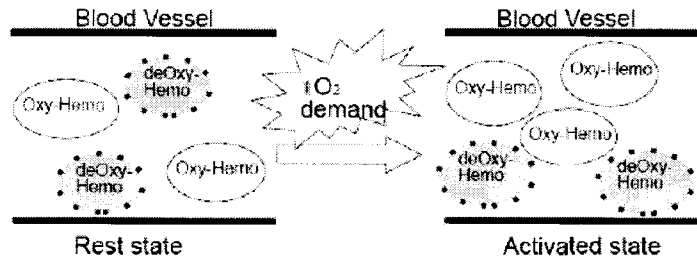


Figure 4.2: Upon neuronal activation, the oxygen demand increases. This leads to the increase in the oxygen level in the blood stream at the activated area to fulfill the need. Since the blood oxygen level affects the MR signal strength, the activation area can be located by comparing the MR signal before and during the neural activation.

shows abnormal brain activity (during seizures) based in EEG. Part of the brain responsible for seizures in patients with epilepsy can also be identified using fMRI. In this case, event-related (ER) fMRI, which performs the image acquisition until the seizures occur, may be used (McRobbie et al. 2006).

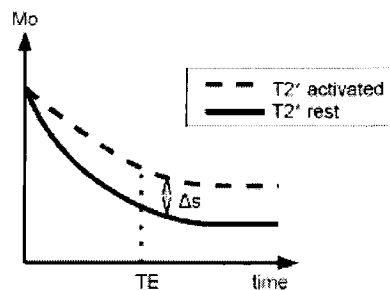


Figure 4.3: Upon neuronal activation, the oxygen demand increases. This leads to the increase in the oxygen level in the blood stream at the activated area to fulfill the need. Since the blood oxygen level affect the MR signal strength, the activation area can be located by comparing the MR signal before and during the neural activation.

The activation map of interest is usually generated off-scanner. There are many ways to analyze the data statistically. General linear models (GLM) are often used in the case of the block design paradigm. The paradigm is assumed to be the expected hemodynamic response function. The assumed hemodynamic response and the measured data are related according to eqn 4.1.

$$Y = \beta \hat{X} + \epsilon \quad (4.1)$$

where Y corresponds to the BOLD measurement, X corresponds to the design matrix (hemodynamic response), β contains parameters to be calculated and ϵ corresponds to the noise matrix.

However, the true hemodynamic response toward any tasks and stimulus are usually not known. To avoid this problem, principle component analysis (PCA) and independent component analysis (ICA) can be used. It is assumed that the variance within a group (either rest state or active state group) is smaller than that between groups. By comparing the variance of the measured data, the activated area can be located.

Although the underlying mechanism of the BOLD effect remains unknown, a functional MR with BOLD effect has been widely accepted as one of the standards for visualizing brain functionality. Repeatable results of the location of brain activation using BOLD functional MRI have been verified using

PET (Gerstl et al. 2008) (R. Peyron and Garcia-Larrea 2000). The application of BOLD in detecting brain function has some advantages: non-ionizing radiation is not required, the activation in any part of the brain may be used, much better anatomical structures are obtained and real time measurements are possible (Buxton 2002).

Indeed, noxious stimulation has been studied using BOLD technique on healthy subjects. It is reported that the thalamus, basal ganglia, insula, somatosensory cortex, cingulate, premotor and motor cortices are activated due to noxious hot (46°C) and noxious cold (5°C) stimulation (Tracey et al. 2000). Other studies of brain response to pain have been done with healthy groups and show similar activation regions, thalamus and sensory cortex, in the brain (R. Peyron and Garcia-Larrea 2000).

The application of BOLD techniques to study the function of the spinal cord has been done successfully (Zhao et al. 2008) (Zhao et al. 2009), although with very high variation, to locate the activation. Due to the small cross-sectional size of the spinal cord, much higher image resolution requirement than that for the brain would be necessary (Stroman et al. 2002). This criterion then restricts the size of the tissue volume being imaged per scan. The spinal cord is more susceptible to susceptibility artifacts than the brain since it is surrounded by bones, cartilage and tissue (Stroman et al. 2008).

Thus, it is not surprising that obtaining high resolution with gradient-echo (GE) and high sensitivity to BOLD effect in the spinal cord is extremely difficult.

Chapter 5

SEEP MRI

5.1 Principles of SEEP MRI

Most MR studies focus on the linearity between BOLD signal and the stimulus. In fact, the relationship between BOLD signal and TE is very important as well. The signal change due to stimulus as a function of TE forms the basis of SEEP MRI. In the past, the BOLD signal as a function of TE has been assumed to be linear with zero intercept. According to chapter 4, BOLD signal is defined as

$$BOLD\ signal = \frac{\Delta S}{S} \quad (5.1)$$

where ΔS corresponds to the signal change due to BOLD effects or BOLD contrast and S corresponds to the rest state MR signal.

Given that the general signal equation of a gradient echo sequence is

$$S = N(H)e^{\frac{-TE}{T2^*}} \sin\theta \frac{1 - e^{\frac{-TR}{T1}}}{1 - \cos\theta e^{\frac{-TR}{T1}}} \quad (5.2)$$

To maximize the T2* weighting, let's assume $\theta = 90$. Thus, $\sin \theta = 1$ and $\cos \theta = 0$. Equation 5.1 becomes

$$\begin{aligned} \frac{\Delta S}{S} &= \frac{N(H)(1 - e^{-\frac{TR}{T_1}})(e^{-\frac{TE}{T_{2*active}}} - e^{-\frac{TE}{T_{2*rest}}})}{N(H)(1 - e^{-\frac{TR}{T_1}})e^{-\frac{TE}{T_{2*rest}}}} \\ &= \frac{e^{-\frac{TE}{T_{2*active}}} - e^{-\frac{TE}{T_{2*rest}}}}{e^{-\frac{TE}{T_{2*rest}}}} \\ &= e^{TE(\frac{1}{T_{2*rest}} - \frac{1}{T_{2*active}})} - 1 \end{aligned}$$

The series expansion of e^{at} , where $a = \text{constant}$, is

$$\begin{aligned} e^{at} &= \sum_{n=0}^{\infty} \frac{at^n}{n!} \\ &= 1 + at + \frac{a^2t^2}{2!} + \frac{a^3t^3}{3!} + \dots \end{aligned}$$

Since $\frac{1}{T_{2*rest}} - \frac{1}{T_{2*active}}$ is a very small number, it is then valid to take the first two terms of the series expansion. The BOLD signal equation can be simplified to be

$$\begin{aligned} \frac{\Delta S}{S} &= 1 + \left(\frac{1}{T_{2*rest}} - \frac{1}{T_{2*active}}\right)TE + \dots - 1 \\ &= \left(\frac{1}{T_{2*rest}} - \frac{1}{T_{2*active}}\right)TE \end{aligned}$$

However, non-zero intercept BOLD response as a function of echo time has been observed by many groups (Liu and Gao 2000) (Pfeuffer et al. 2003) (Jin et al. 2006). It has been shown that fractional signal change ($\delta S/S$) has

a non-zero intercept and non linear function in Figure 5.1 below (Stroman et al. 2002) (Stroman 2005) (Stroman et al. 2002). Based on this result, the Stroman group proposed that the second effect may be a result of the proton density changes in the spinal cord upon neuronal activity. This second effect, signal enhancement by extravascular proton (SEEP), is independent of the BOLD effect and corresponds to the changes in the proton density in the extravascular system during the neural activation.

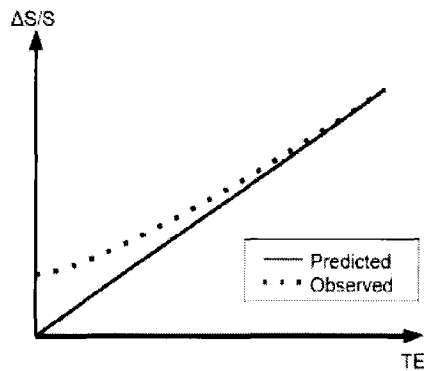


Figure 5.1: The BOLD signal as a function of TE. The dotted line corresponds to the observed non-linear function. The solid line corresponds to the linear function predicted. The non-zero intercept is observed with the non linear function.

SEEP mechanism may be explained using two physiological proofs. Blood flow and perfusion increase during neural activation may promote the unidirectional water flow during neural activation. This is observed in the brain using position emission tomography (PET) with radiolabelled water tracer (Stroman 2005). Also, the shrinkage and swelling of the cell in response

to neural activation have been demonstrated by Stroman et al. . Indeed, there is not only ionic exchange during the transportation of the neural signal (action potential); water is also transported into and out of the cell at the same time (Stroman et al. 2008).

The high resolution requirement in spinal cord fMRI leads to the low signal to noise ratio (SNR) due to the small voxel size used. Due to the size of the spinal cord, it would be expected that the sagittal view would suffer from partial volume effect more seriously than the coronal and transverse views (Figley and Stroman 2007). Pulsatile flow of cerebral spinal fluid, breathing and surrounding tissue movement may induce motion artifacts. Conventional motion correction techniques such as respiration gating, cardiac gating and fluid-attenuated inversion recovery (FLAIR) sequence show limited improvement in the resultant image (Figley and Stroman 2009). Stroman et al, proposed a noise reduction technique by applying the retrospective spinal cord motion time-course estimates (RESPITE), based on the principle components of the spinal cord motion, as a physiological noise regressor in the GLM analysis (Figley and Stroman 2007) (Figley and Stroman 2009). The proposed noise reduction technique is able to reduce the percentage of false positives and increase the detection sensitivity.

Unfortunately, it is very difficult to reproduce a good result with SEEP technique. Such techniques have been applied in healthy groups and show promising results in locating the activation inside the spinal cord (Stroman et al. 2008). Zhao F et al (2008) shows that BOLD and body-volume weighted techniques may be applied to study the spinal cord upon noxious stimulation (A-fibers) but not non-noxious stimulation (C-fibers) in rat models. In other words, no activation in the spinal cord would be expected when the temperature stimulus is in the range of 15° to 42° ; the response to the temperature stimulus would be observed only in the brain. The brain activation pattern differences between patients undergoing chemotherapy and a healthy group responding to the temperature stimulus have not been studied.

Chapter 6

Diffusion Tensor Imaging (DTI)

6.1 Principles of DTI

The mobility of molecules in solution may be described by the diffusion coefficient (D). Generally, the movement of free water molecules can be described by random walking in thermodynamic theory (i.e. it is a Gaussian distribution). Mathematically speaking, the spread of free water molecules can be assumed to be isotropic (Mori 2007). In the presence of cellular structures, the motion of water may be directional (anisotropic case in mathematical terms). When a gradient pulse pair shown in figure 6.1 is applied, the pulse pairs flip the spins to 180° clockwise then 180° anti-clockwise (Hashemi et al. 2003).

No change in the MR signal should be expected in the case of stationary spins. If the spins are in directional motion, additional exponential attenuation of the signal would be produced, which may be described using Eq (6.2)

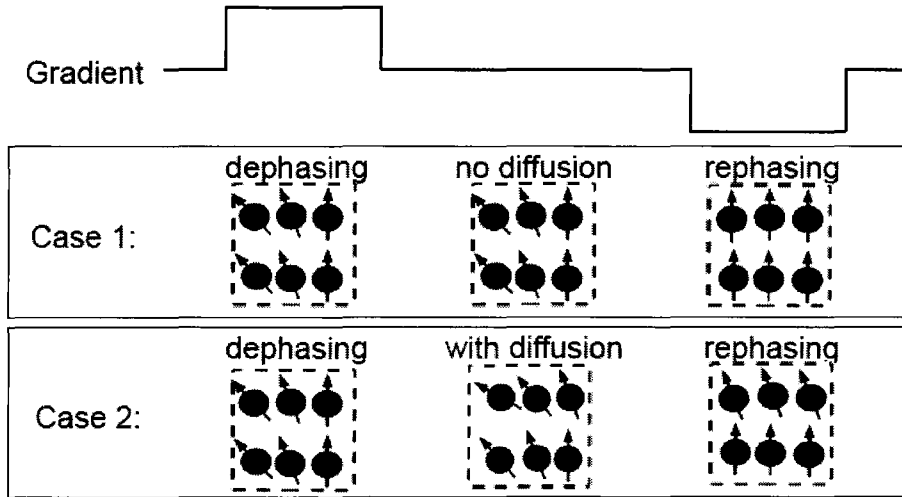


Figure 6.1: The gradient pulse pair consists of a dephasing gradient and a rephasing gradient. The rephasing gradient undo the effect of the dephasing gradient. In the case of no diffusion (case 1), no change in the spin should be observed before experiencing the rephasing gradient. For simplicity, let's assume diffusion process being a 1D problem where the first row of the spins moved to the right. The rephasing gradient thus fails to realign all the spins. The signal in case 1 is then stronger than that in case 2.

$$\frac{S}{S_0} = e^{-\gamma^2 G^2 \delta^2 (\Delta - \delta/3) D} \quad (6.1)$$

$$= e^{-bD} \quad (6.2)$$

,where G is the strength of the gradient pulse, δ is the duration of the pulse, Δ is the time between the gradient pulse pair, b is an arbitrary parameter that incorporates the amplitude and timing parameter of the gradient. D is the

apparent diffusion coefficient (ADC). S is the signal detected and S_0 is the signal.

D corresponds to the slope of the signal attenuation as a function of b -value in semi-log scale. The simplest way to calculate D requires two sets of signal attenuation and b -values. There is no signal attenuation when $b = 0$ s/mm² (T2-weighted image). At any b -value there is diffusion weighting and attenuation of the resultant spin echo. The ADC is calculated according to 6.2 (Hashemi et al. 2003) Since the motion of water molecules is in 3 dimensions, D is characterized as a diffusion tensor(DT) matrix instead of one single value. It is worth knowing that the DT matrix is diagonalizable. As illustrated below, D_{ij} equals to D_{ji} . (i.e. $D_{xy} = D_{yx}$, $D_{xz} = D_{zx}$, $D_{yz} = D_{zy}$)(Mori 2007) In this case, only 7 measurements would be needed (6 signal attenuation measurements for DT matrix and 1 signal attenuation measurement for at $b=0$).

$$D = \begin{bmatrix} D_{xx} & D_{xy} & D_{xz} \\ D_{yx} & D_{yy} & D_{yz} \\ D_{zx} & D_{zy} & D_{zz} \end{bmatrix}$$

Mathematically speaking, ADC represents the variance of the water motion in all directions. It is expected that CSF, which has free mobilized water molecules, has high ADC values (appears white in ADC map). White matter

and grey matter, where water migration is restricted by the cell structure, have low ADC values (appear dark in ADC map). The fractional anisotropy (FA) is a mathematical quantity ranging from 0 to 1. (refer to equation 6.3).

$$FA = \sqrt{\frac{3}{2} \frac{\sqrt{(\lambda_1 - \langle \lambda \rangle)^2 + (\lambda_2 - \langle \lambda \rangle)^2 + (\lambda_3 - \langle \lambda \rangle)^2}}{\sqrt{\lambda_1^2 + \lambda_2^2 + \lambda_3^2}}} \quad (6.3)$$

,where λ corresponds to the eigenvalues based on the DT matrix.

It describes the shape of the fiber based on the motion of water molecules. When FA equals 0, isotropic geometry is obtained. (Water molecules travel the same distance at all directions) When FA equals 1, anisotropic geometry is obtained. (All water molecules travel in a specific direction) For example, white matter has a long cylindrical structure. The FA value of white matter is high. The water molecules in CSF are relatively mobile. The FA value of CSF is low. The diffusivity may be calculated using the diffusion weighted image (DWI). Unlike the DTI, DWI requires less measurement. (Only the D_{xx} , D_{yy} , D_{zz} are measured.) The diffusivity parameters determined based on DWI are more likely to be affected by the position of the patient and are less reproducible (Buxton 2002) (Clark and Werring 2002) (Bihan et al. 2002).

The choice of b-value can be critical for optimum signal to noise ratio (SNR). If b-value is set to be too large, signal intensity measured is small. Poor SNR will result. If b-value is set to be too small, the signal decay will be too

small to be detected (Mori 2007). The situation can be even more complicated since the optimal b-value depends on the orientation of the fiber structure as well (Mori 2007). Different b-values should be used for different part of the body. The calculation of D assumes the the signal attenuation as a function of b-values in semi-log scale to be linear. Although this is not completely true, this approximation gives reasonable prediction on diffusion parameters. Some researcher suggests that significant change in diffusion constants occurred when b-value greater than 3000s/mm^2 , rather than b-value less then 3000s/mm^2 , is applied (Mori 2007).

Common b-values used for clinical study fall in the range from 600 to 1200 s/mm^2 (Mori 2007). In case of the brain, b-value is usually set to be around 700s/mm^2 to 1000s/mm^2 (Naganawa et al. 2004). Optimal b-values in case of the spinal cord DTI are not well determined. High b-value and low b-value, 1500s/mm^2 and 650s/mm^2 respectively, have been proposed as the optimal choice. Typically, low b-value (around 650s/mm^2) is used for reasons such as shorter scan time, reasonable SNR and reduction of ghosting due to spinal cord motion (Summers et al. 2006). High b-value setting, however, shows better identification of diffusion dynamic, particularly the slow diffusion process. When the water movement may be slow in the MR time scale due to the present of microstructural barriers. The application of higher b-value (

$>1500 \text{ s/mm}^2$) would allow a better quantification of the water moving into and out of the microstructures (Farrell et al. 2008). On the other hand, high b-value setting shows poor SNR, more susceptible to motion artifacts and eddy current distortion.

Due to the structure and location of the spine, it is hard to measure its activity or to image the spine non-invasively. The mechanism involved in the spine is not well understood. The spinal cord activation measurement may be done by inserting a probe into the vertebral column (Clark and Werring 2002). Obviously, this is a risky method where the subject may suffer from permanent spine injury. Noninvasive spinal cord imaging may be done with traditional MRI, which is usually carried out for diagnosis of spinal cord injury. Research has been done to investigate the possibility of diagnosing spinal cord injury based on the fiber tracking data and the change in the ADC map (Clark and Werring 2002) (Bihan et al. 2002).

Although DTI technique is not yet applied in clinical situations, the potential of using DTI in diagnosing brain and spinal cord abnormalities has drawn great attention. The recent studies are focused on the application of fiber tracking to look at spinal cord injury (Bammer and Fazekas 2003) (Tsuchiya et al. 2005). DTI has also been done to look at the changes in diffusivity in the brain or spinal cord of patients with various disorders

such as multiple sclerosis (Bammer and Fazekas 2003) (Quasthoff and Hartung 2002) and children with leukemia, (Quasthoff and Hartung 2002) which may be done by comparing the ADC value and FA value. Recently, Porto et al looked at the DT and FA difference between long-term survivors with childhood leukemia and healthy subjects and showed the reduction in white matter and grey matter concentration in the brain of these survivors (Porto et al. 2008). Together with the findings that the white matter concentration correlates with brain development in children and IQ, (Mabbott et al. 2006) the findings by Porto's group may explain the cognitive change in acute lymphoblastic leukemia survivors who are treated with both chemotherapy and radiotherapy or chemotherapy alone. However, the difference between CIPN patients and a healthy group in terms of their ADC and FA values has not been studied.

Chapter 7

Statement of the Problem and Hypotheses

7.1 Current Issues

During the course of cancer therapy, damage to the surrounding healthy tissue is unavoidable. In the case of chemotherapy, the drug used is designed to target tumor cells and not to pass through the blood brain barrier (BBB). However, there have been numerous reports describing sensory changes and short term memory loss in patients receiving chemotherapy. In the lay literature this effect is commonly referred to as chemobrain. Even though the chemotherapy agents are not supposed to cross the BBB, the prevalence of chemobrain implies the contrary, or the agent may somehow affect BBB function leading to chemobrain. Regardless of how the mechanism works, there is no doubt that chemobrain results in a degradation in the quality of life.

In the past, treatment efficacy was the physician's primary concern while side effects such as pain and discomfort were less important. Although cognitive change is also observed in patients undergoing brain radiotherapy

and/or surgery, it is the chemotherapy patients who experience a more dramatic and earlier onset of brain changes. Up until recently the presence of CIPN was generally ignored and any cognitive changes were usually disregarded as a psychological or emotional issue in dealing with cancer.

As evidence supporting the reality of CIPN is magnified, and public concern about the quality of life of cancer patient has been elevated and attention toward the causes, mechanism and cure of CIPN has also been increased. Current research on CIPN mainly focuses on the location of the side effects and on the drug that is responsible. Some scientists describe so called 'proof' for CIPN based on frequently observed peripheral nerve demyelination, one side effect observed with many chemotherapeutic agents (Custodio 2008) (Quasthoff and Hartung 2002) (Wickham 2007). However, the effect of chemotherapeutic agents on the central nervous system (i.e. brain and spinal cord) is still not understood. Scientists have suggested many theories on the cause of CIPN. For example, some suggest the chemotherapeutic agent somehow interacts with either the structure or function of the BBB. With the cause of CIPN still not known, and a cure currently unavailable, more research is needed to understand the mechanism(s), and prevention/cure of CIPN.

7.2 Hypothesis

Some theories suggest that CIPN occurs due to axonal loss in PNS. All chemotherapy agents are designed so that they do not pass through the BBB. It is assumed, by theory, that the chemotherapy agents do not affect the brain. Based on the clinical findings, such as short term memory loss in chemo-brain patients, changes must be occurring in the CNS as well. At this moment, the parts of the nervous system affected by chemotherapy agents are not known.

The best approach to non-invasively evaluate the CNS is through use of advanced MRI techniques. A combination of diffusion tensor imaging (DTI) and functional MRI (fMRI) allow detailed evaluation of brain structure and function, respectively. Furthermore this combination enables for better pathological localization (if any) relative to any other imaging approach. CIPN patients are either abnormally sensitive to temperature or abnormally insensitive to temperature. In this work, four temperature settings were applied. These settings are applied to differentiate the temperature response between healthy volunteers, hypersensitive CIPN patients and hyposensitivity CIPN patients. Temperature settings within the non-noxious temperature range were chosen. It was hypothesized that hypersensitive CIPN patients have lower temperature threshold. Furthermore, the brain activation pattern between above and

below temperature threshold stimuli should be different. The hyposensitive CIPN patients are assumed to have higher temperature threshold. No difference in the brain activation pattern among the four temperature settings should be observed. Similarly, healthy volunteers should have no difference in the brain activation pattern between the four temperature settings.

Using DTI for assessment of tissue structure, change in FA values can be interpreted as change in white matter integrity. It is hypothesized that CIPN patients will also show differences in brain structural characteristics. Furthermore, it is hypothesized that areas having greater changes in DTI metrics will correlate with areas that have aberrant sensitivity to temperature stimulation, as measured with fMRI.

Chapter 8

Method Development

This chapter describes the development of the protocol, which would be potentially useful in detecting the functional changes in CIPN patients. All scans are done with the GE Signa HD 3T short-bore MR imaging system (General Electric Healthcare, Wilwaukee, WI), which is located at the Imaging Research Center of the Brain-Body Institute, St. Joseph's Healthcare, Hamilton, Ontario, Canada.

8.1 Spinal cord fMRI

The location of the major affected areas in the nervous system that lead to the sensory changes in CIPN patients is not known. To verify if the sensory stimulus transportation was affected before reaching the brain, spinal cord fMRI was conducted using SEEP technique and images were acquired using an 8 channel CTL-spinal cord surface coil (General Electric Healthcare, Wilwaukee, WI). Changes in the activation pattern as well as the associated amplitude should be observed if chemotherapy agents affect the peripheral ner-

vous system and/or the spinal cord. High resolution anatomic imaging(2D-AX-FAST-SPRG) of the cervical spinal cord was first acquired axially (18 slices, TE/TR = 1/300ms, 15 flip angle, 4mm thickness, 0 skip, 256x256 matrix.). The functional images were then acquired using the same FOV as the 3D anatomic image sagittally using a fast spin echo sequence without cardiac gating (6 slices, TE/TR = 40/2000ms, 90 flip angle, 3mm thickness, 0mm skip, 128x128 matrix, 43 phases). A block designed non-noxious stimulation was applied onto the right palm of one healthy subject using a tooth brush (as shown in figure 8.1).

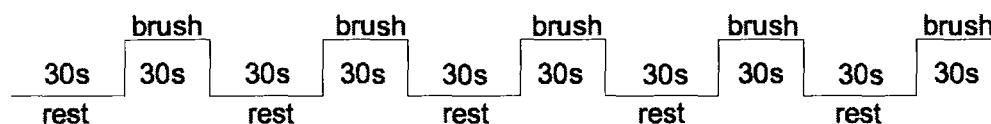


Figure 8.1: Non-noxious stimulation(brushing) timing diagram that is used for Spinal cord fMRI with SEEP technique

The SEEP images were analyzed using a FEAT tool from FSL (FMRIB Centre, Department of Clinical Neurology, University of Oxford). A simple block design paradigm (30s ON 30s OFF) was used for the GLM analysis. Figure 8.2 shows the z-score map overlay on the anatomical image. If activation inside the spinal cord was detected, most activation (red dots) should be observed inside the spinal cord. The scattered activation pattern suggests that the observed activation could be noise.



Figure 8.2: The sagittal image of the same subject at different slice. The resulting activation pattern was thresholded using uncorrelated voxel method with threshold set at $p=0.01$. No significant activation is observed inside the spinal cord using SEEP sequence. Some activations are observed inside the spinal cord as well as in the muscle outside the spinal cord.

A similar approach was then taken using EPI sequences. Functional images were acquired sagittally (5 slices, TE/TR=35/2000ms, 90 flip angle, 1.6mm thickness, 0 skip, 256x224 matrix) using CTL-spine surface coil. Non-noxious stimulation was performed using a tooth brush. Analysis was done with the FEAT tool in FSL the same way as the SEEP technique. Again, no significant activation inside the spinal cord was observed (refer to figure 8.4 below).



Figure 8.2: The sagittal image of the same subject at different slice. The resulting activation pattern was thresholded using uncorrelated voxel method with threshold set at $p=0.01$. No significant activation is observed inside the spinal cord using SEEP sequence. Some activations are observed inside the spinal cord as well as in the muscle outside the spinal cord.

A similar approach was then taken using EPI sequences. Functional images were acquired sagittally (5 slices, TE/TR=35/2000ms, 90 flip angle, 1.6mm thickness, 0 skip, 256x224 matrix) using CTL-spine surface coil. Non-noxious stimulation was performed using a tooth brush. Analysis was done with the FEAT tool in FSL the same way as the SEEP technique. Again, no significant activation inside the spinal cord was observed (refer to figure 8.4 below).

For better SNR, an 8-channel Head/C-spine coil (General Electric Healthcare, Wilwaukee, WI), which allows ASSET, was used. EPI scan of the spinal cord from C5 to T1 was then performed axially(5 slices, TE/TR=35/2000ms, 90 flip angle, 2.4mm thickness, 0mm skip 64x64 matrix, 30 phases). Non-noxious stimulation (tooth brush) was applied during the functional scans with no cardiac gating. A block design paradigm that follows figure 8.1 was used. Unfortunately, no significant activation was observed after the analysis using FEAT tool in FSL program.

It was expected that noxious temperature stimulation (temperature greater than 46° or less than 15°) would produce a larger change in the BOLD signal. Noxious stimulation had been performed on the right palm of a health subject based on a block designed paradigm. Corresponding functional images were acquired axially using EPI sequence. A timing paradigm similar to that shown in the previous section (figure 8.3) was used.

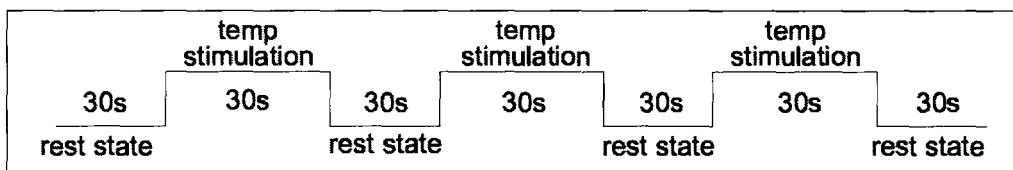


Figure 8.3: The timing diagram used for the noxious stimulation (ice pack). It is expected that a stronger BOLD signal can be generated.

The noxious stimulation was applied using an ice pack. Note that a difference sequence was used to acquire anatomical spine images using the 8-

channel Head/C-spine coil (3D-IR-prepped fSPGR, TE/TR/TI = 20/3300/720ms, flip angle = 90, slice thickness = 4mm, 256x256 matrix). As shown in the z-score map generated using the FEAT tool in FSL ($p = 0.01$), however, the activation was observed inside as well as outside the spinal cord (refer to figure 8.4).

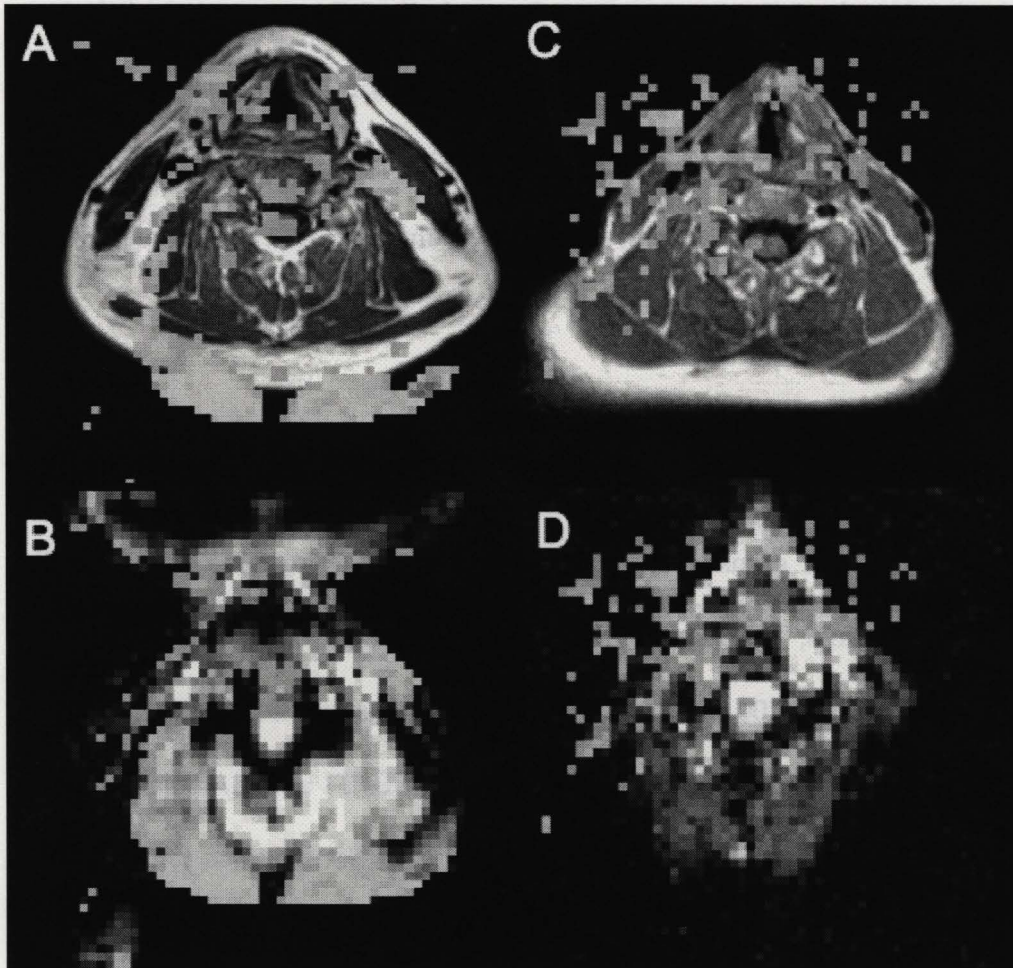


Figure 8.4: Axial images of the spinal fMRI using EPI sequence. Figure A and B corresponds to the non-noxious stimulation (brushing on the right palm). The anatomical image is placed by the z-score map in figure A and the same z-score map is placed on top of the raw EPI image in figure D. Figure C and D corresponds to the noxious stimulation (placing an ice-pack on the right palm). The z-score map is placed on top of the anatomical image in figure C and the same z-score map is placed on top of the raw EPI image in figure D. In both cases (brushing on right palm or placing ice-pack on right palm), activation patterns outside the spinal cord were observed.

The failure in detecting a signal using spinal cord fMRI may be explained using the following reasons. First of all, different statistical design may be used by Stroman's group. Secondly, digital filters was applied in the data presented by Stroman's group. Difference in digital filter design and post-processing of the MR signals may lead to the failure of SEEP technique in this work.

8.2 Brain fMRI using Ramped Stimulus

Brain fMRI scans on two healthy volunteers were done using a EPI sequence (30 slices, TE/TR = 35/3000ms, 90 flip angle, 5mm thickness, 0mm skip, 64x64 matrix, 100 phases) following the high resolution brain anatomical scan (3D-IR-prepped fSPGR, 31 slices, TE/TR/TI = 2/6/450ms, 90 flip angle, 1.6mm thickness, 0 skip, 128x128 matrix). Non-noxious temperature stimulation ranging from 21°C to 35°C was applied on a healthy subject using the temperature stimulation system as shown in figure 8.5.

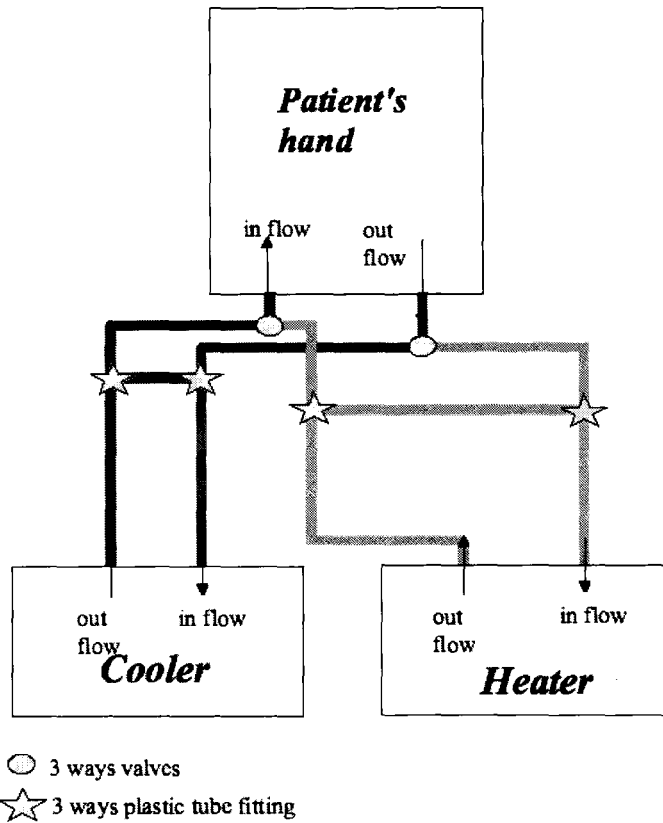


Figure 8.5: Schematic of the temperature stimulating system that produces ramping stimulation. By controlling the inflow and the outflow switch, the hot/cold water flows to the patient and leads to increase/decrease in temperature

An alternating water flow toward the right palm of the subject was done at a two-minutes interval, which resulted in a ramping temperature stimulation pattern (figure 8.6).

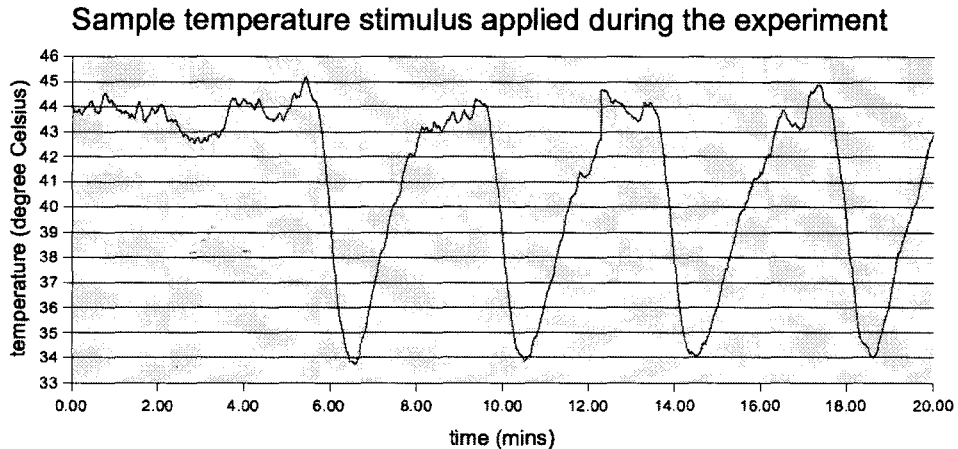


Figure 8.6: Sample temperature measurement during the experiment

Instead of a two minutes ON and two minutes OFF block design, the real time temperature on the surface of the water coil was detected by the T-type implantable thermocouple then measured by Powerlab (ADInstruments Pty Ltd, Bella Vista, Australia). The real time temperature measurement was used as the ideal function for the GLM analysis. However such sensors failed to provide accurate temperature readings during the scans. Signal fluctuation caused by interference with the MR sequence was observed. Relative temperature measurement was then done as an alternative to absolute temperature measurements.

Based on the GLM analysis using FSL, no voxels seem to be following the assumed hemodynamic model. Figure 8.7 is the time course of BOLD signal of the voxel showing the best fit to the predefined hemodynamic model. Obviously, the result does not show good alignment.

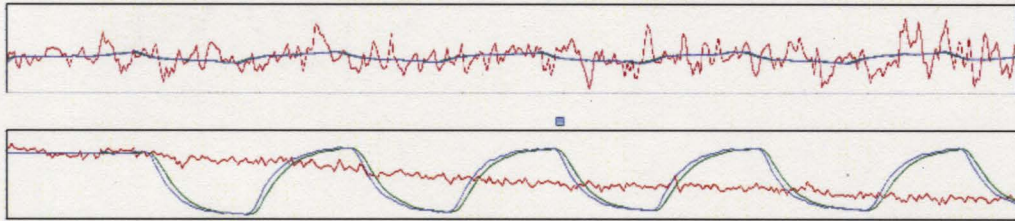


Figure 8.7: The time course of BOLD signal of the voxel with the best fit to the predefined ideal wavefront. Block paradigm (top time course) or real time measurement (bottom time course) were used as the hemodynamic response function during the GLM calculation. The blue, green and red lines correspond to actual the full model fit, cope partial model fit and the actual data, respectively. Neither the block paradigm or the real time measurement generate reasonable BOLD signal fit.

8.3 Brain fMRI using Blocked stimulus

8.3.1 Block design comparison (2mins ON 2mins OFF vs 30s ON 30s OFF)

The failure in the ramp stimulation may be associated with hemodynamic habituation, where the brain fails to respond to the change in signal due to over-activation. In order to confirm this hypothesis, block stimulus with

Based on the GLM analysis using FSL, no voxels seem to be following the assumed hemodynamic model. Figure 8.7 is the time course of BOLD signal of the voxel showing the best fit to the predefined hemodynamic model. Obviously, the result does not show good alignment.

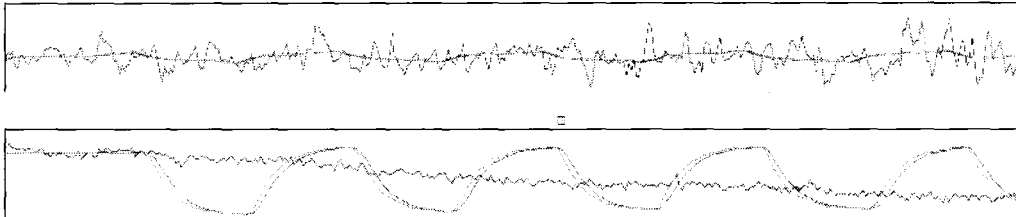


Figure 8.7: The time course of BOLD signal of the voxel with the best fit to the predefined ideal wavefront. Block paradigm (top time course) or real time measurement (bottom time course) were used as the hemodynamic response function during the GLM calculation. The blue, green and red lines correspond to actual the full model fit, cope partial model fit and the actual data, respectively. Neither the block paradigm or the real time measurement generate reasonable BOLD signal fit.

8.3 Brain fMRI using Blocked stimulus

8.3.1 Block design comparison (2mins ON 2mins OFF vs 30s ON 30s OFF)

The failure in the ramp stimulation may be associated with hemodynamic habituation, where the brain fails to respond to the change in signal due to over-activation. In order to confirm this hypothesis, block stimulus with

the two stimulation patterns were performed. In one of the stimulations, the noxious temperature stimulation was applied on the right palm of the healthy volunteer for thirty seconds then away from the right palm for thirty seconds. The other stimulation was done with two minutes on the right palm of the subject then two minutes away from the healthy volunteer. The later case was performed to give a stimulation time period similar to the ramp stimulation case (refer to figure 8.8). EPI sequences (31 slices, TE / TR = 35 / 3000ms, 90 flip angle, 5mm thickness, 0mm skip, 64x64 matrix, 100 phases) were performed with a fixed noxious temperature stimulation (50°C) on the two healthy volunteers (Hot water was running inside the water coil to produce a fixed surface temperature of 50°C.). Noxious temperature setting was chosen to improve the SNR. T-type implantable thermocouples provided by Powerlab was used to monitor the surface temperature of the water coil.

Figure 8.9 gives the averaged BOLD signal time course of two scans. Clearly, the averaged BOLD signal follows the ideal wavefront better in the 30s ON 30s OFF block design. The activation in the sensory cortex was observed with the 30s ON 30s OFF block design as well.

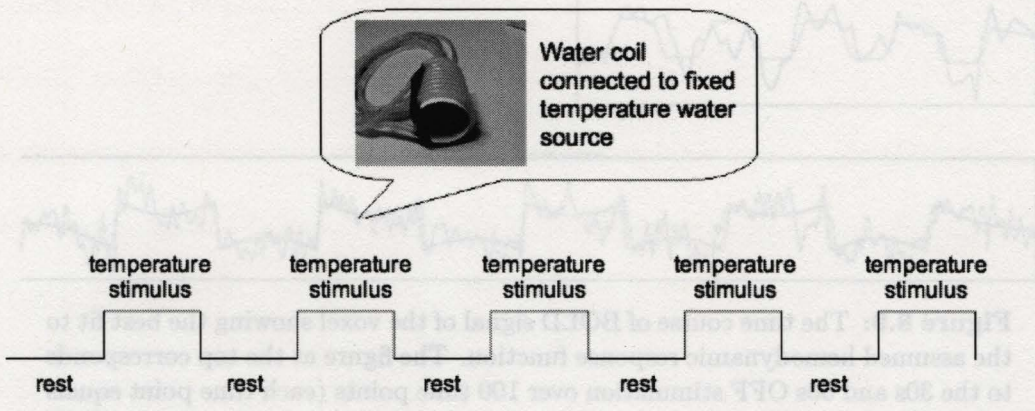


Figure 8.8: Noxious stimulation(fixed 50°C) timing diagram that is used for spinal cord fMRI with EPI technique. Two sets of fMRI scan were done.(30s rest and 30s temperature stimulus cycle and 2 minutes rest and 2 minutes temperature stimulus cycle.)

8.3.2 non-noxious temperature stimulation

At any temperature below the noxious temperature (46°), the same areas of the brain should be activated (thalamus and somatosensory cortex). It was also observed previously that the BOLD signal measured with non-noxious stimulation was small. The temperature sensitivity difference between subject may varies. The fMRI result of one of the temperature settings could be noisy. Repeating the BOLD measurement with a series of non-noxious temperatures increased the sample size. This should increase the reliability of the fMRI result. EPI sequences (31 slices, TE/TR = 35/3000ms, 90 flip angle, 5mm thickness, 0mm skip, 64x64 matrix, 100 phases) were performed following the high resolution anatomical brain scan (3D-IR-prepped fSPGR, 31 slices,

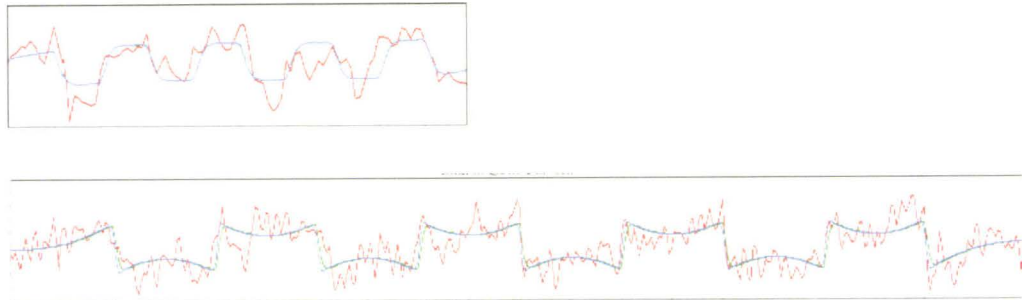


Figure 8.9: The time course of BOLD signal of the voxel showing the best fit to the assumed hemodynamic response function. The figure at the top corresponds to the 30s and 30s OFF stimulation over 100 time points (each time point equals to 1 TE). The figure at the bottom corresponds to the 2min ON and 2min OFF stimulation over 400 time points (each time point equals to 1 TE). The blue, green and red lines correspond to the full model fit, cope partial model fit and the actual data, respectively.

TE/TR/TI= 2/6/450ms, 90 flip angle, 1.6mm thickness, 0 skip, 128x128 matrix). A series of block stimuli was performed with 4 non-noxious temperature settings(12°C, 21°C, 35°C, 40°C) on a CIPN patient and healthy subjects. Temperature settings within the non-noxious temperature range were chosen. Due to the system limitation, 12°C is the lowest achievable temperature setting. While 21°C and 35°C are close to the room temperature and the patient's body temperature, respectively. It is hypothesized that hypersensitive patients show higher BOLD signal and have different hot pain threshold. If the pain threshold of the hypersensitive CIPN patients was lower than temperature stimulus. Activation pattern corresponds to pain should be observed among the hypersensitive CIPN patients. None of the temperature settings (12°C, 21°C, 35°C and 40°C) should induce pain activation pattern among the

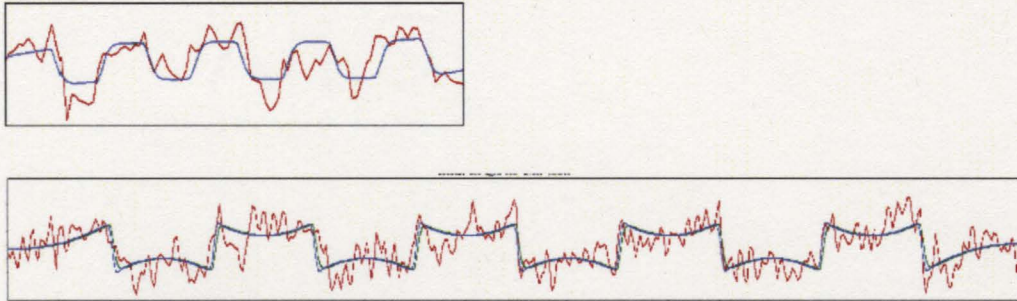


Figure 8.9: The time course of BOLD signal of the voxel showing the best fit to the assumed hemodynamic response function. The figure at the top corresponds to the 30s and 30s OFF stimulation over 100 time points (each time point equals to 1 TE). The figure at the bottom corresponds to the 2min ON and 2min OFF stimulation over 400 time points (each time point equals to 1 TE). The blue, green and red lines correspond to the full model fit, cope partial model fit and the actual data, respectively.

TE/TR/TI= 2/6/450ms, 90 flip angle, 1.6mm thickness, 0 skip, 128x128 matrix). A series of block stimuli was performed with 4 non-noxious temperature settings(12°C, 21°C, 35°C, 40°C) on a CIPN patient and healthy subjects. Temperature settings within the non-noxious temperature range were chosen. Due to the system limitation, 12°C is the lowest achievable temperature setting. While 21°C and 35°C are close to the room temperature and the patient's body temperature, respectively. It is hypothesized that hypersensitive patients show higher BOLD signal and have different hot pain threshold. If the pain threshold of the hypersensitive CIPN patients was lower than temperature stimulus. Activation pattern corresponds to pain should be observed among the hypersensitive CIPN patients. None of the temperature settings (12°C, 21°C, 35°C and 40°C) should induce pain activation pattern among the

healthy volunteers and the hyposensitive CIPN patients. Weak BOLD signal should be observed in the hyposensitive CIPN patients for all four temperature settings. The increment of the temperature stimulation also ensure the effectiveness of the stimulus. The surface temperature of the water coils was measured using Neopticx TM optical signal conditioners (Quebec City, Quebec, Canada), which show a more reliable temperature during each scan. Since manual temperature offset was still used to reach the designated temperatures, a temperature fluctuation of $\pm 2^\circ$ was achieved based on experience. To reduce the experimental time, two water sources were used and connected to two separate water coils as shown in figure 8.10

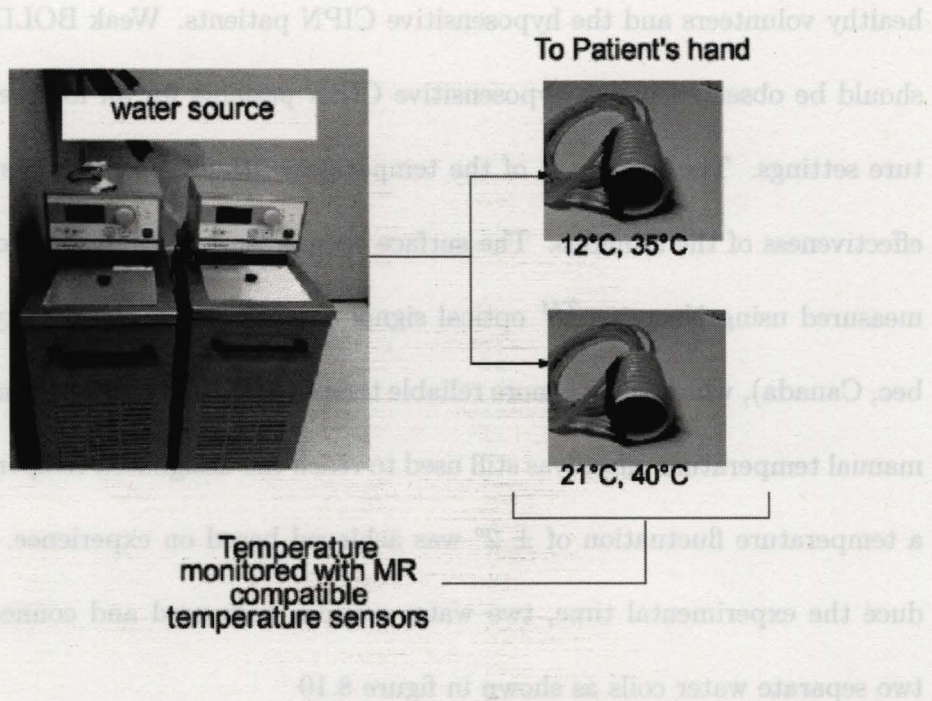


Figure 8.10: Experimental set up of the temperature stimulation system for block designed temperature stimulation

To avoid hemodynamic habituation, alternately three seconds on the hand and two seconds off the hand were repeated during the thirty seconds course of temperature stimulation. This procedure is critical in order to minimize the chance of hemodynamic habituation. As shown in figure 8.11 below, the dotted line corresponds to the actual temperature stimulus and the solid line corresponds to the assumed hemodynamic response. Such protocol had been performed on the right palm and the right forearm of a healthy subject to determine the location of the hand with better temperature sensitivity.

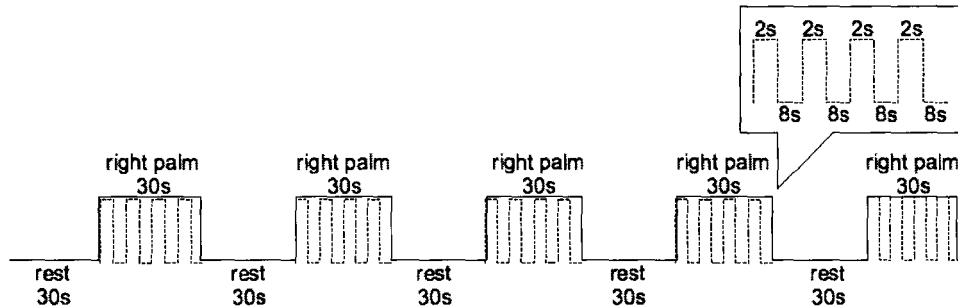


Figure 8.11: Temperature stimulus timing diagram that was used for 4 different non-noxious temperature settings. The solid line corresponds to the assumed hemodynamic response for GLM analysis and the dotted line corresponds to the actual stimulus timing.

Multiple regression analysis was done using AFNI (NIMH, Bethesda, MD USA). Sensory cortex has high F-test value across the temperature settings. (refer to 8.12).

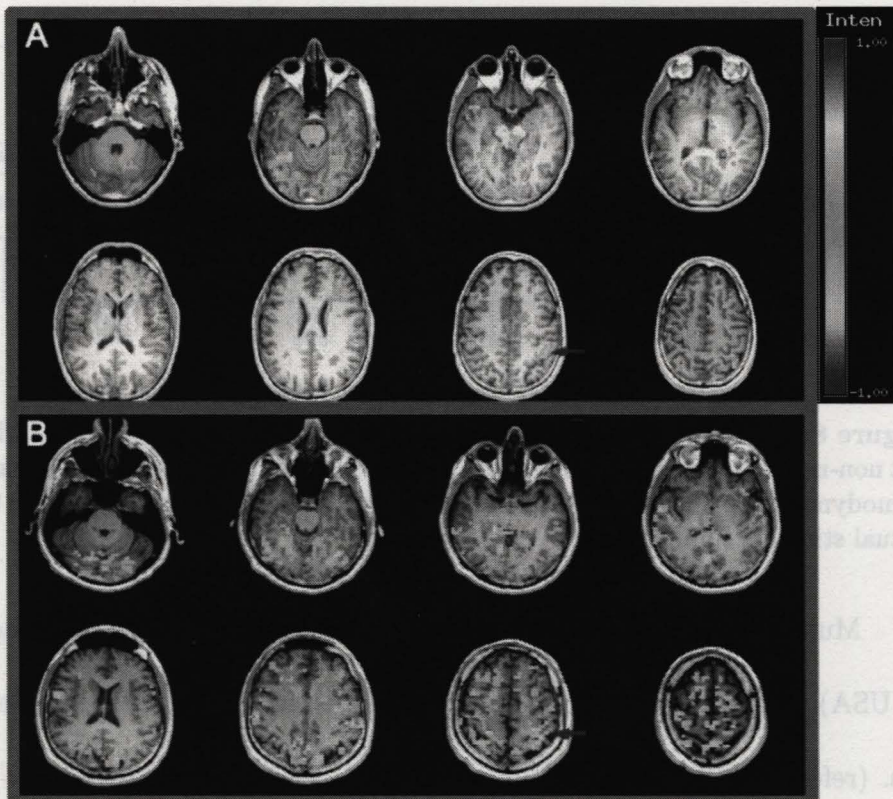


Figure 8.12: The F-test result from the multiple regression analysis on two healthy volunteers. (subject A: $p = 1.2 \times 10^{-3}$, $F = 4.59$. subject B: $p = 1.2 \times 10^{-3}$, $F = 4.59$) It shows that the activation at the sensory cortex (indicated using red arrow) is highly correlated across all 4 temperature settings.

Since exciting results were obtained, a repeatability test was performed on the one subject on three different days. Similar brain activation pattern was obtained on the same subject. (refer to 8.13)

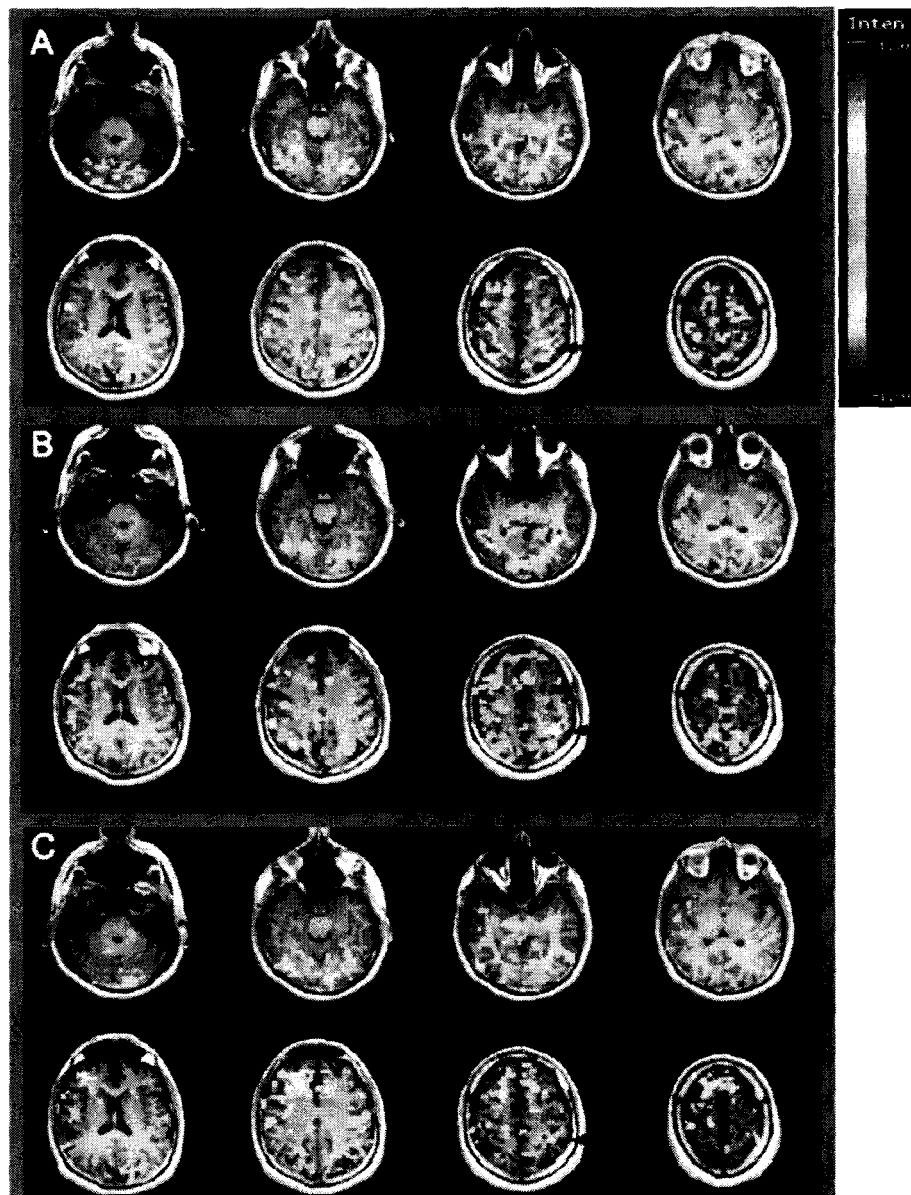


Figure 8.13: The F-test result map of the same subject (thresholded at $p=1.2 \times 10^{-3}$, $F=4.59$) imaged on three different dates. Similar activation was observed on the sensory cortex.(indicated using red arrow)

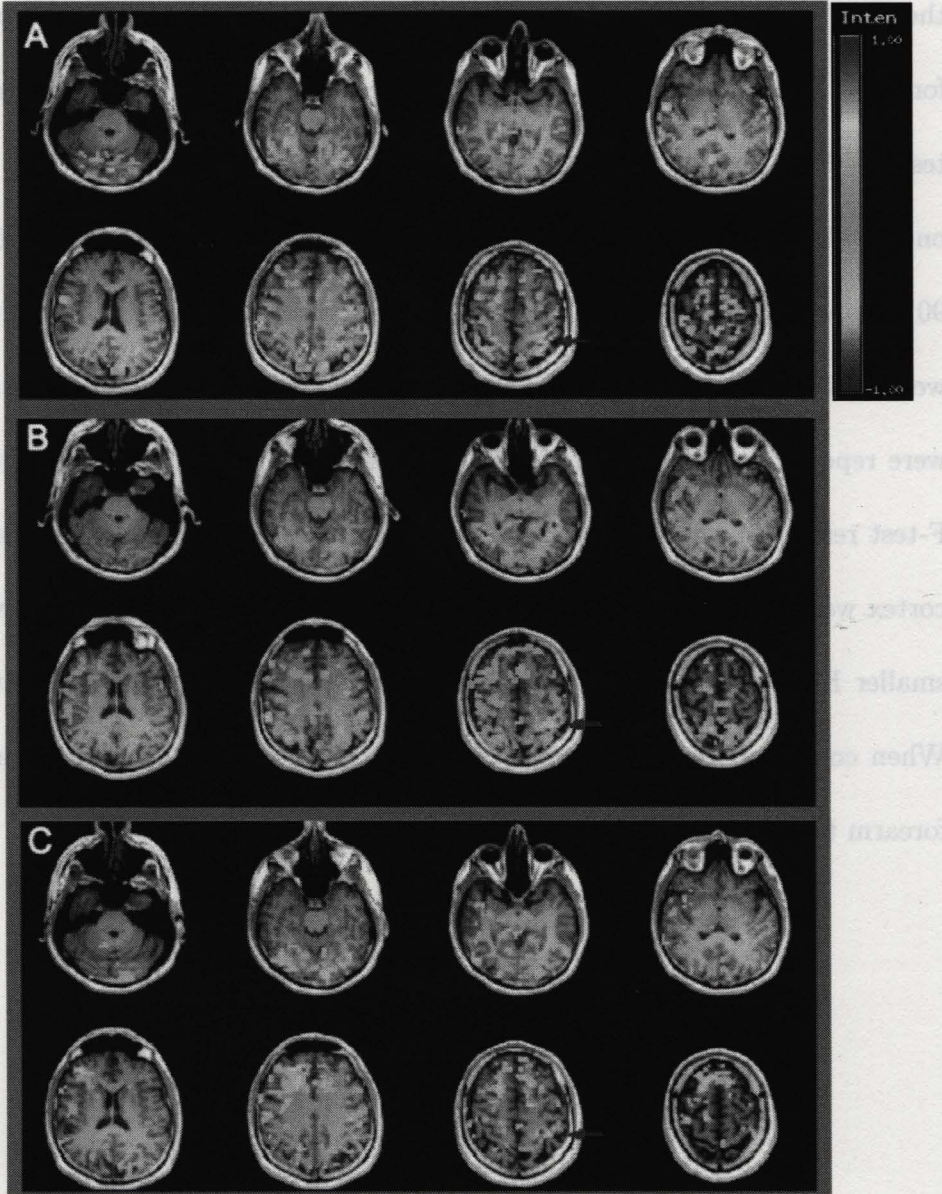


Figure 8.13: The F-test result map of the same subject (thresholded at $p=1.2 \times 10^{-3}$, $F=4.59$) imaged on three different dates. Similar activation was observed on the sensory cortex.(indicated using red arrow)

Since the skin on the forearm is not as thick as the skin on the palm, the SNR could be further improved by performing the temperature test on the forearm. The temperature sensitivity between the palm and the forearm was tested. The temperature sensitivity between the palm and the forearm was tested. The same temperature settings (12°C, 21°C, 35°C, 40°C) were done on a healthy volunteer using EPI fMRI scan (30 slices, TE/TR = 35/3000ms, 90 flip angle, 5mm thickness, 0mm skip, 64x64 matrix, 100 phases). The scans were first performed on the right palm of the volunteer. The same fMRI scans were repeated on the right forearm of the same volunteer. According to the F-test result shown in figure 8.14, higher F-test values in the somatosensory cortex were obtained with the forearm case. When the BOLD signal is weak, smaller F-test result should be found among the four temperature settings. When compared the response to forearm activation to palm activation, the forearm test results gave better result.

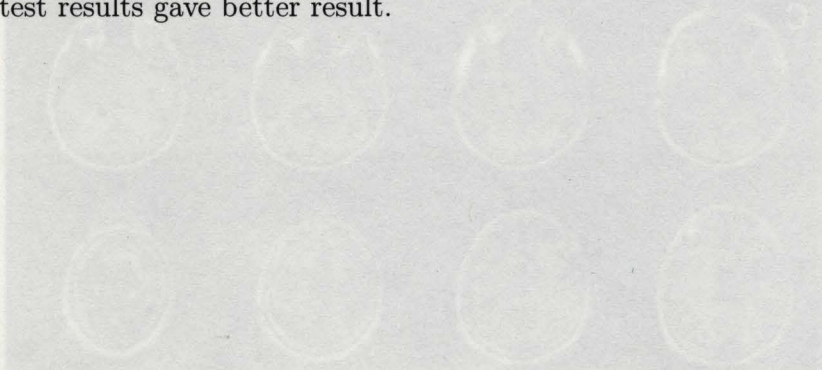


Figure 8.13: The F-test result map of the same subject (thresholded at $p=1.5 \times 10^{-4}$, $F=4.50$) imaged on three different dates. Similar activation was observed on the sensory cortex (indicated using red arrow).

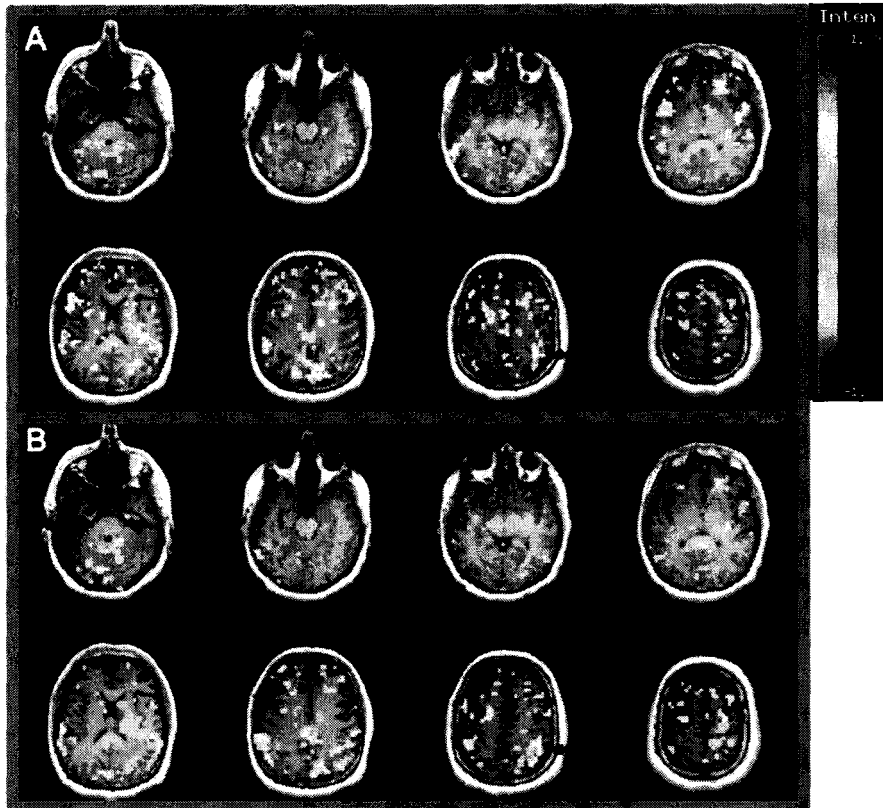


Figure 8.14: The F-test result from the multiple regression analysis based on the test results was done on the same healthy volunteer on the same day. (thresholded at $F = 3.7$, $p = 3.5 \times 10^{-2}$) Figure A corresponds to the test done on the palm. Figure B corresponds to the test done on the forearm. Stronger correlations in the somatosensory cortex (indicated using red arrow) were obtained in the forearm case.

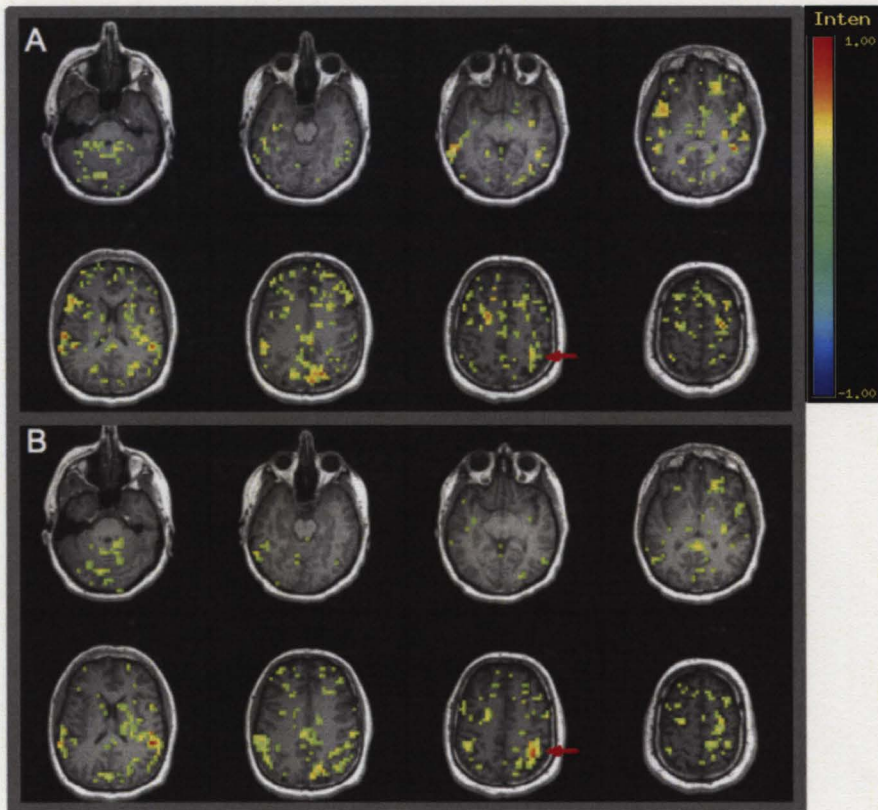


Figure 8.14: The F-test result from the multiple regression analysis based on the test results was done on the same healthy volunteer on the same day. (thresholded at $F = 3.7$, $p = 3.5 \times 10^{-2}$) Figure A corresponds to the test done on the palm. Figure B corresponds to the test done on the forearm. Stronger correlations in the somatosensory cortex (indicated using red arrow) were obtained in the forearm case.

Chapter 9

Materials and Methods

9.1 DTI in the brain and spinal cord

9.1.1 Data Acquisition

Both spinal cord and brain DTI scans were done using a diffusion weighted spin echo EPI sequence. For the brain DTI scan (TR=10000ms, NEX=3, FOV=256x256, b=900, direction=25, slice thickness = 3mm, 0 skip, $b = 900 \text{ s/mm}^2$), the whole brain was imaged. The resultant image set had the same FOV as the high resolution 3D anatomical brain images (3D-IR-prepped fSPGR, 31 slices, TE/TR/TI = 2/6/450ms, 90 flip angle, 1.6mm thickness, 0 skip, 512x256). Two sets of spinal cord DTI scans (direction =15, FOV=128x128, NEX=4, slice thickness = 5mm, 0 skip, 10 RR-interval) were done axially using b-values equal to 650 s/mm^2 or 1500 s/mm^2 . Since the spinal cord DTI scans were cardiac gated, the corresponding high resolution 3D spinal cord anatomical imaging (3D-IR-prepped fSPGR, TE/TR/TI =

2/6/450ms, 90 flip angle, 1.6mm thickness, 0 skip, 256x224 matrix) was done with a different number of slices. Nevertheless, both DTI scans had the same FOV and all images (both DTI and the 3D anatomical images) acquired were done in a way such that C6 to C7 of the spinal was covered.

9.1.2 Data Analysis

Image pre-processing was done using AFNI, FSL and diffusion toolkit (Athinoula A. Martinos Center for Biomedical Imaging, Charlestown, Massachusetts).

Separate masks that contain the region of interest (ROI) in the brain, i.e. the white matter and grey matter, were first created using the high resolution anatomical images. This would, hopefully, increase the accuracy of the mask. The white matter and grey matter masks were generated after skull stripping using the brain extraction tool and segmentation tool in the FSL program. However, direct application of these masks to the DTI images could be problematic. Thus, the linear transformation matrix was then obtained by registering the high resolution anatomical image to the $b=0$ s/mm^2 DTI image. This matrix was then applied to the masks using the linear registration tools in the FSL program.

FA, eigenvalues and ADC values were calculated based on the brain DTI images using AFNI after motion correction and eddy current correction (using FSL program). The mean FA, eigenvalues and ADC values of each ROI (white matter and grey matter of the brain) were compared between healthy volunteer groups and CIPN patients using a t-test. Voxel-based analysis between the healthy volunteers and the CIPN patients was also performed after registering all the brain images to the Talairach space.

The volume of the spinal cord was relatively small when compared with the acquired image. The parameters, such as FA, eigenvalues and ADC values, of the whole spinal cord were calculated. Although ROI analysis could be possible. This would result in a reduction in the number voxel for the calculation. It was then more appropriate to create the spinal cord masks using the $b=0$ s/mm² DTI image. Group analysis was done by comparing the mean FA, eigenvalues and ADC values using a t-test.

9.2 fMRI in the brain

9.2.1 Temperature stimulation systems

The temperature stimulation systems consisted of three main components: two water sources, two water coils and a temperature monitor system. The design of the system is shown in figure 8.10 of the previous chapter.

The water sources in the temperature stimulating system came from two VMRTM signature Heated circulators 1167P (VMR International, Breakfast Creek, Australia). Each water circulator contained an internal temperature sensor, which allows temperature stability to be $\pm 0.01^{\circ}\text{C}$ in a closed circulation setting. The circulators allowed controlling the temperature using external temperature or internal temperature sensors. Delay in the temperature feed back may be resulted if external temperature sensors were used. Therefore, internal temperature control was used during all the experiments with manual offset at the temperature setting. Another set of temperature measurements of the water coils were recorded using an external temperature sensor (NeoptixTM) to allow a better estimation in the manual offset setting. Temperature stimulation was generated by placing the water coil on the forearm and the palm of the volunteer. The control over the water coil surface

temperature was more critical than the temperature of the water flowing inside the water coil.

NeoptixTM optical signal conditioners, which allow temperature measurement with accuracy of $\pm 0.8^{\circ}\text{C}$, were used to monitor and record the temperature at the surface of the water coils, room temperatures and the surface temperature of the palm of the subjects. It was very hard to maintain a constant surface temperature of the water coil during the functional task. The surface temperature of the water coil depends on environmental factors such as room temperature and the skin temperature of the patient. Generally speaking, the water was heated to 2 to 3 $^{\circ}\text{C}$ above the target temperature. During the temperature fMRI scans, the water would then be cooled several degrees Celsius below the target temperature (The process would be reverse for 12 $^{\circ}\text{C}$ setting. Increase in water temperature resulted during the temperature fMRI scans). This, thus, compensated for the change in the coil surface temperature when the coil was placed on the patient. Based on the temperature recorded during each experiment, the temperature fluctuation of the stimulus with this method is $\pm 2^{\circ}\text{C}$.

9.2.2 Data Acquisition

It has been observed that the forearm has higher temperature sensitivity in normal subjects. However, the test for diagnosing CIPN is done on the palm. Therefore, it makes sense to perform the stimulus on both the palm and the forearm. The temperature stimulus was, thus, modified such that it was applied for thirty seconds on the right palm and thirty seconds on the left forearm as shown in Figure 9.1 below. This way, no additional scanning was necessary. For improvements on the image quality, the matrix size of the anatomical scan was modified from 128x128 to 512x256 (The parameters now became: 3D-IR-prepped fSPGR, 31 slices, TE/TR/IT = 2/6/450ms, 90 flip angle, 1.6mm thickness, 0 skip, 512x256).

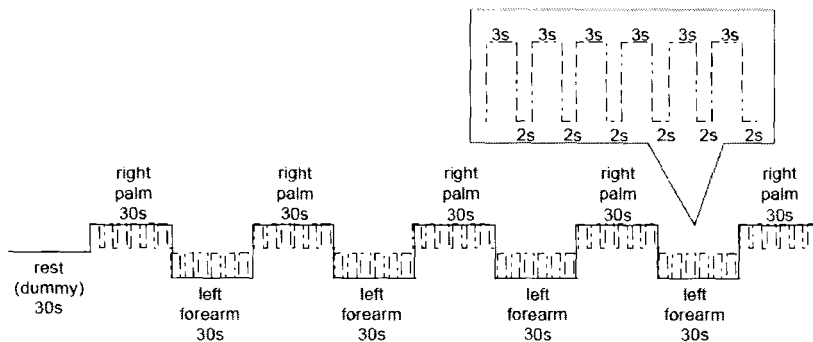


Figure 9.1: Modified temperature stimulus timing diagram that was used for 4 different non-noxious temperature settings. Temperature stimulus was applied alternately on the right palm and the left forearm of the same patient. The solid line corresponds to the assumed hemodynamic response for GLM analysis and the dotted line corresponds to the actual stimulus timing.

An additional motor fMRI scan was also performed during the experiment. A finger-tapping motor task was performed by the patient during the EPI scan (31 slices, TE/TR = 35/3000ms, 90 flip angle, 5mm thickness, 0mm skip, 64x64 matrix, 100 phases), which had the image FOV and parameters as the temperature fMRI scan described above. A five minute motor task was performed in a thirty seconds OFF then thirty seconds ON block design paradigm. The hemodynamic response between subjects are different. The additional motor fMRI scans can be served as a reference. For example, a healthy volunteer tends to show low BOLD response to motor task if he/she shows low BOLD response to temperature stimulations. In this case, the motor fMRI results would be useful in justifying the unexpected result. The motor functional scan results are also useful to show the preservation of the motor function in CIPN patients. Note that all the functional and anatomical images covered the same area of the brain.

9.2.3 Data Analysis

Image post processing and statistical analysis were all done with AFNI. After the motion correction and spatial smoothing, voxel by voxel deconvolution analysis of individual fMRI time series data was done. Multiple linear regression analysis was performed and an F-map was generated that showed

the correlation across all four temperatures applied. An ANOVA test was performed on the healthy volunteer group as well. Unfortunately, there were not enough CIPN volunteers to perform any statistical analysis between the healthy group and the CIPN patient group. However, statistical comparison (two tail unpaired t-test) was performed between the healthy and CIPN patient volunteers based on the results obtained from the motor fMRI scan.

9.3 Subject Selection

Before any clinical trial, the protocol was tested with five healthy male volunteers in the age range from 25 to 39 years. After testing the protocol on the healthy volunteers, two male and one female CIPN volunteers (in the age range from 50 to 67 years) were recruited for the study. They all fulfilled the requirements stated below.

1. Patient received chemotherapy drugs, such as platinum compounds, vinca alkaloids, taxols and suramin, during the course of their cancer treatment.
2. Patient developed CIPN for more than two months.
3. Patient had an Eastern Cooperative Oncology Group (ECOG) score less than or equal to 2 and a Karnofsky's Performance score of 60 or higher.

Among those CIPN patients, one patient reported hypersensitivity to temperature and the other two patients reported hyposensitivity to temperature.

Chapter 10

Results and Discussion

10.1 DTI in the brain and spinal cord

DT images are more susceptible to motion and eddy current distortion than 3D anatomical images. As a result, the shape of the acquired DT images are slightly different from that of the 3D anatomical image. Motion correction, eddy current correction, linear registration and non-linear registration are common tools to reshape the DT image. In this study, however, the combination of motion correction, eddy current correction and linear registration gave reasonable registration results. Generally, registering low resolution images (DT image in this case) to high resolution images (3D anatomical in this case) are discouraged. Any transformation may slightly modify the value of each voxel in the resulted image. Thus, the high resolution ROI masks are registered to the lower resolution DT images. Given that non-linear registration refines the alignment of the fine structure inside the brain, relatively small adjustments are usually involved. The non-linear registration would not necessarily give better results than that using linear registration for the purpose

of this study. Furthermore, the application of linear registration show good coverage and mapping of the white and grey matter (refer to Figure 10.1). No further adjustments was necessary. Thus, non-linear registration was not performed.

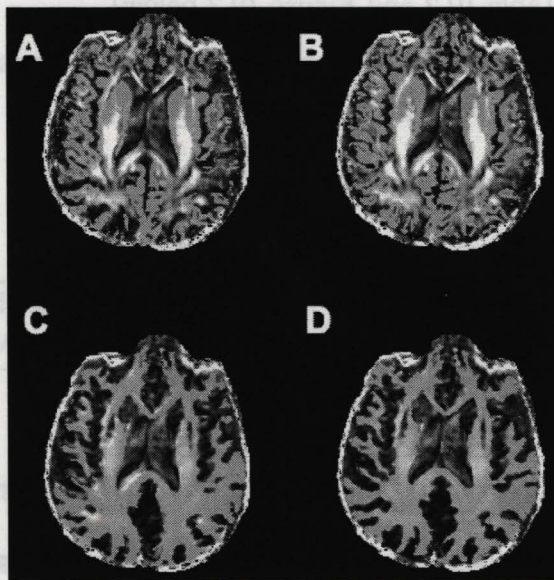
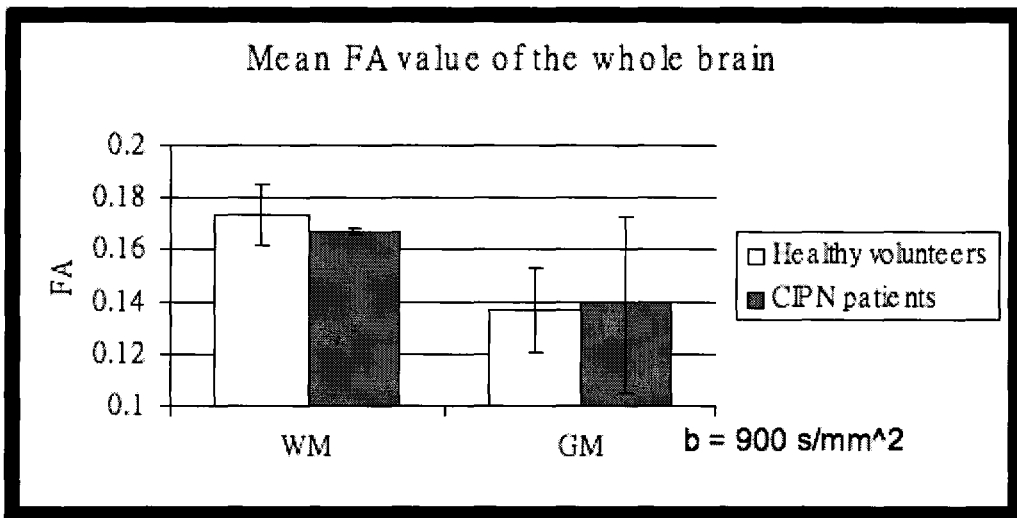
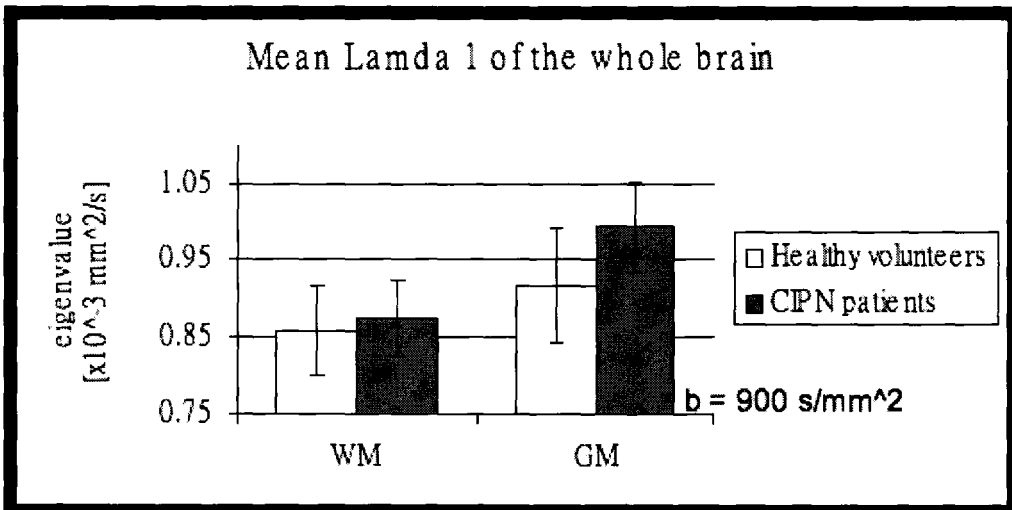
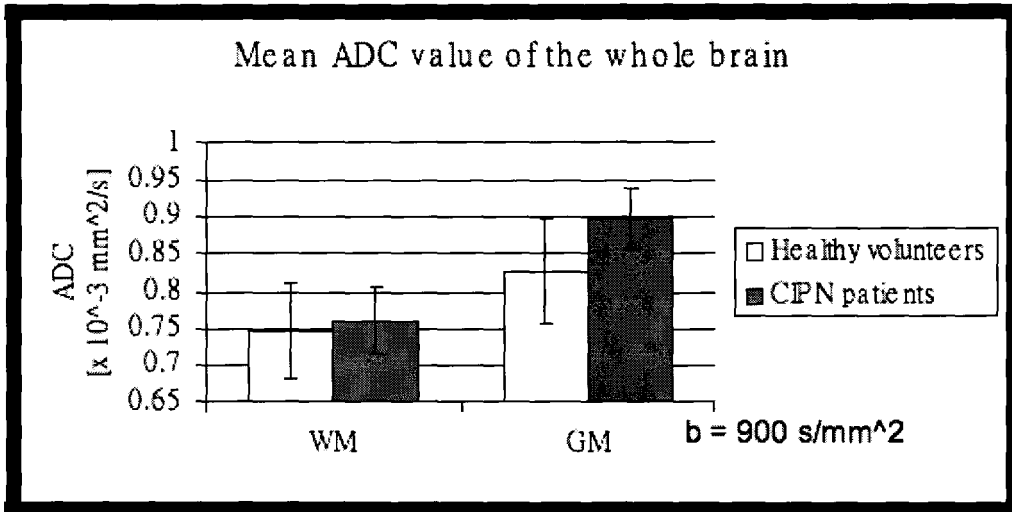


Figure 10.1: All four figures above are obtained from the same subject at the same location. Figure A and C correspond to the masked FA map before applying the linear registration. Figure B and D correspond to the linearly transformed masked FA map. Both grey matter masks (Figure A and B) and white matter masks (Figure C and D) show improvement in localization after the application of linear transformation.

When performing the ROI analysis on the brain DTI data, all the CIPN patients were assumed to show similar diffusivity characteristics. The mean and the standard deviation of the diffusivity parameters (FA, mean ADC and mean eigenvalues (λ_1 , λ_2 and λ_3)) of each group were first calculated. A t-

test was performed to compare these mean values of the healthy volunteers (5 subjects, in the age range of 25 to 39) to those of CIPN patients (3 subjects, in the age range of 50 to 67). No significant difference in FA, ADC and eigenvalues were observed between the healthy volunteers and CIPN patients. (refer to Table 10.1, Table 10.2 and Figure 10.2 below).





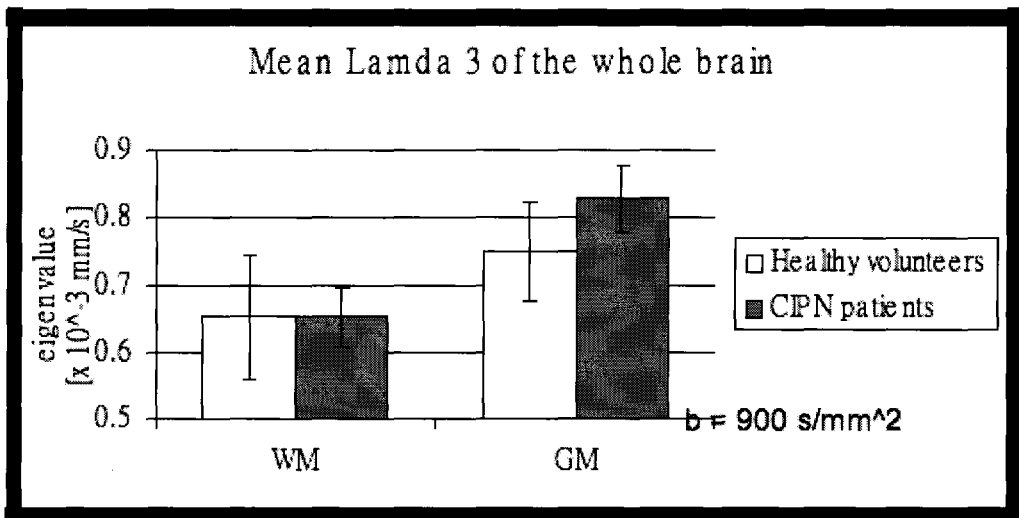
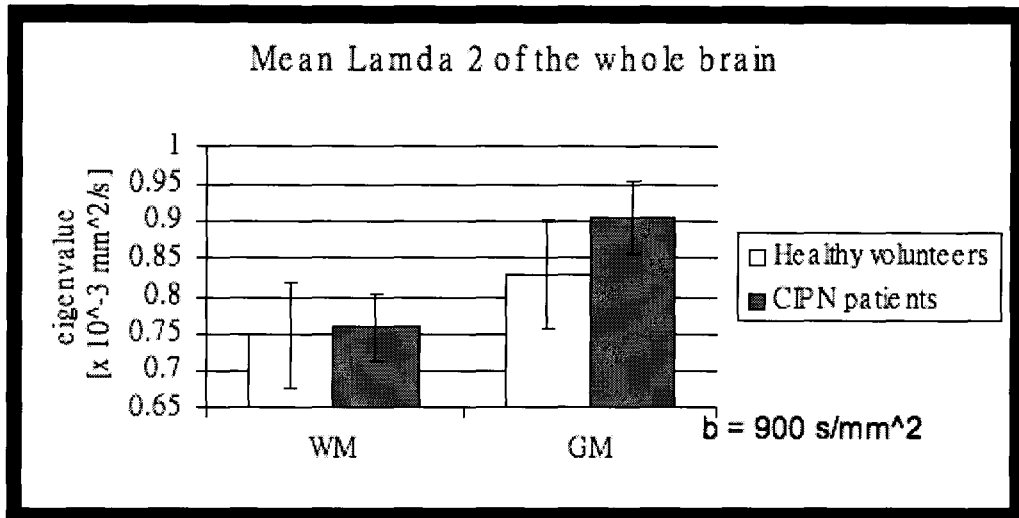


Figure 10.2: The plots of the mean and standard deviation (represented as the error bars) of FA, ADC and eigenvalues (λ_1 , λ_2 and λ_3) using ROI analysis (white matter (WM) and grey matter (GM) of the whole brain). The scans are done with $b = 900\text{s/mm}^2$. No difference between the healthy volunteers and the CIPN patients are observed based on the FA, ADC and eigenvalues of the white matter and grey matter obtained in this study.

	Healthy volunteers		CIPN patients	
	White Matter	Grey Matter	White Matter	Grey Matter
FA	0.17±0.01	0.14±0.02	0.17±0.00	0.14±0.03
ADC [x 10³ mm²/s]	0.75±0.07	0.83±0.07	0.76±0.05	0.90±0.04
λ1 [x 10³ mm²/s]	0.86±0.06	0.92±0.07	0.87±0.05	0.90±0.04
λ2 [x 10³ mm²/s]	0.75±0.07	0.83±0.07	0.76±0.05	0.91±0.05
λ3 [x 10³ mm²/s]	0.65±0.09	0.75±0.05	0.65±0.00	0.83±0.05

Table 10.1: The result from the brain DTI ROI (white matter and grey matter of the whole brain) analysis result. The mean values and the standard deviation of FA, ADC and eigenvalues (λ_1 , λ_2 and λ_3) of each ROI are determined. All scans are done with $b = 900\text{s/mm}^2$.

	White Matter	Grey Matter
FA	1.09	0.16
ADC [x 10³ mm²/s]	0.33	1.83
λ1 [x 10³ mm²/s]	0.46	1.74
λ2 [x 10³ mm²/s]	0.24	1.84
λ3 [x 10³ mm²/s]	0.01	1.84

Table 10.2: t-test result based on the brain DTI result. The scans are done with $b = 900\text{ s/mm}^2$. The mean FA, ADC and eigenvalues from healthy volunteers and CIPN patients are compared. No significant difference is observed. ($p=0.05$ level of significant is 2.447)

Decrease in FA value have previously been reported in the white matter of the brain among breast cancer survivors (Abarham et al. 2008). Abraham et al studied the effect of adjuvant chemotherapy of early diagnosed breast cancer patients . Ten breast cancer survivors, who were suffering from cognitive changes after chemotherapy, and 9 age and education-matched healthy

volunteers were recruited. Based on their ROI (at the genu of the corpus callosum), decrease in white matter integrity was observed in patients.

Unfortunately, the above result is not observed in this study. There are a few differences in the experimental setup, which might be useful in explaining the observations. First of all, the recruited healthy volunteer in this study are not age, sex and education matched with the CIPN patient. Secondly, ROI analysis at the genu of the corpus callosum was done in Abarham's study. White matter of the whole brain was used in this study. Sullivan et al 2006 studied the difference in FA values in different sex and age group. Decrease in FA values of the white matter in the brain as the age increases. The change in the FA value also depends on the location of the brain and the characteristics of the fibers inside the ROI. For example, the FA values in the ROI containing mostly white matter are different from the ROIs containing mixture of white matter and grey matter.

Using voxel based morphometry (VBM) results, no differences in the FA, ADC and eigenvalue were observed between the healthy volunteers and CIPN patients. It was expected that a certain region of the brain, such as the white matter, would show a significant t-score. However, as shown in figures below (Figure 10.3, Figure 10.4, Figure 10.5 , Figure 10.6 and Figure 10.7) none of the t-statistic maps of the FA, ADC and eigenvalues provided any

significant t-test result in a group inside the brain. The unexpected results in both the VBM and ROI analysis may be biased due to the age difference and the limited sample size.

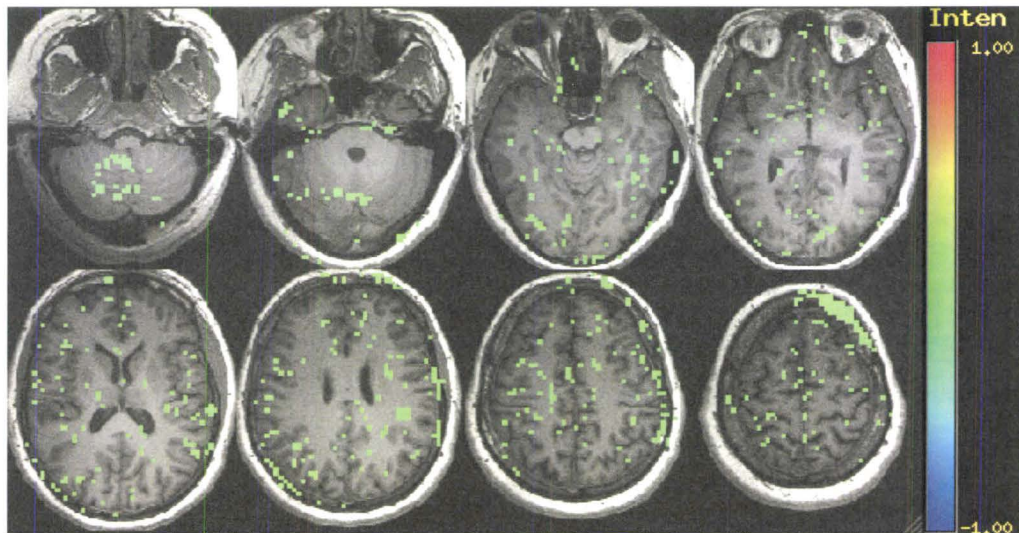


Figure 10.3: The t-score maps (thresholded at $t\text{-score} = 2.44$, $p = 0.0505$) based on the VBM result. Voxel by voxel FA value comparison between the healthy volunteers and CIPN patients was done.

significant t-test result in a group inside the brain. The unexpected results in both the VBM and ROI analysis may be biased due to the age difference and the limited sample size.

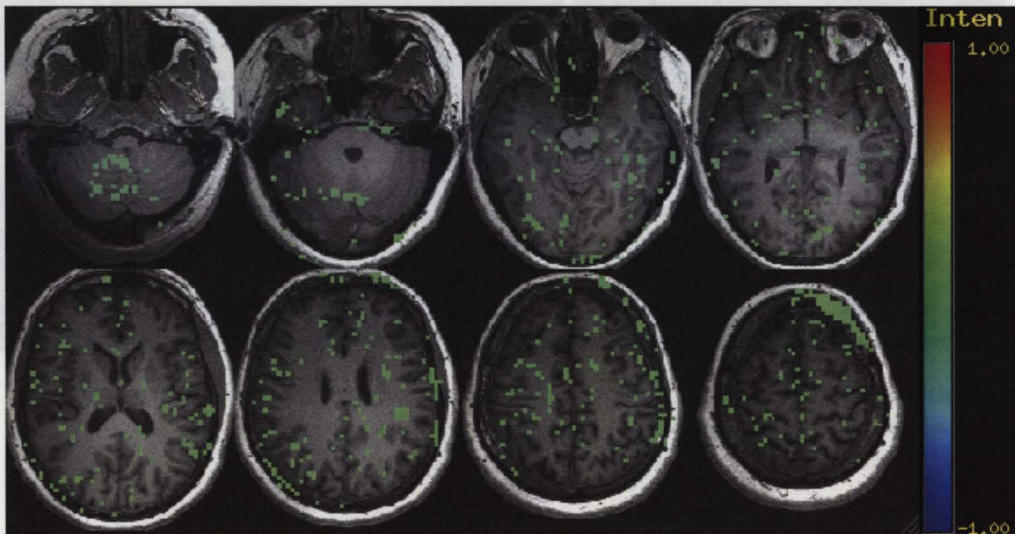


Figure 10.3: The t-score maps (thresholded at t-score = 2.44, $p = 0.0505$) based on the VBM result. Voxel by voxel FA value comparison between the healthy volunteers and CIPN patients was done.

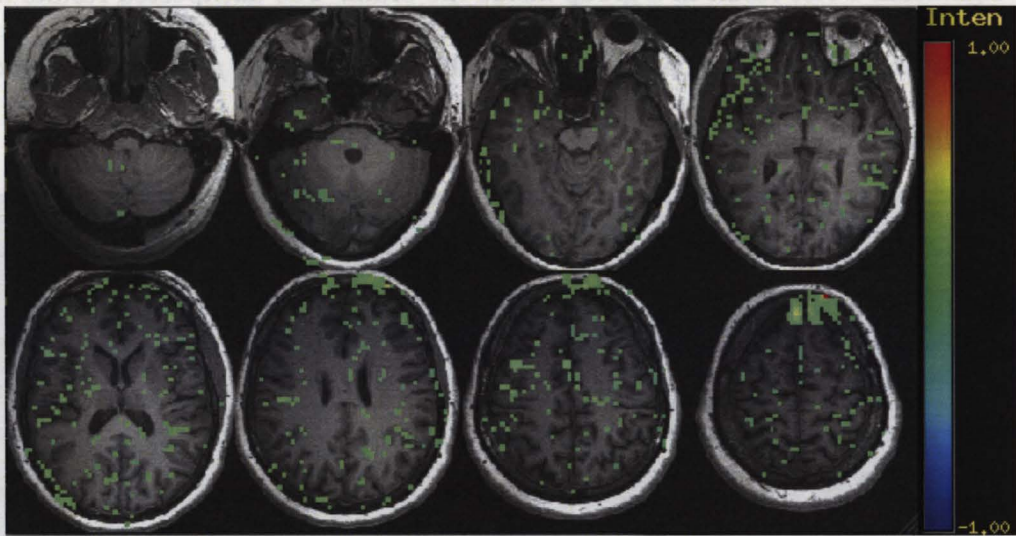


Figure 10.4: The t-score maps (thresholded at $t\text{-score} = 2.44$, $p = 0.0505$) based on the VBM result. Voxel by voxel ADC value comparison between the healthy volunteers and CIPN patients was done.

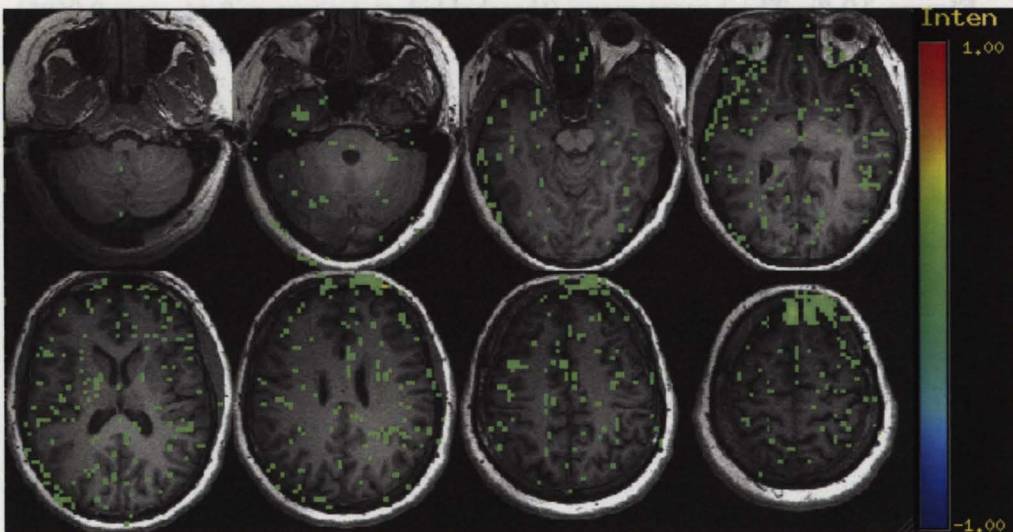


Figure 10.5: The t-score maps (thresholded at $t\text{-score} = 2.44$, $p = 0.0505$) based on the VBM result. Voxel by voxel λ_1 value comparison between the healthy volunteers and CIPN patients was done.

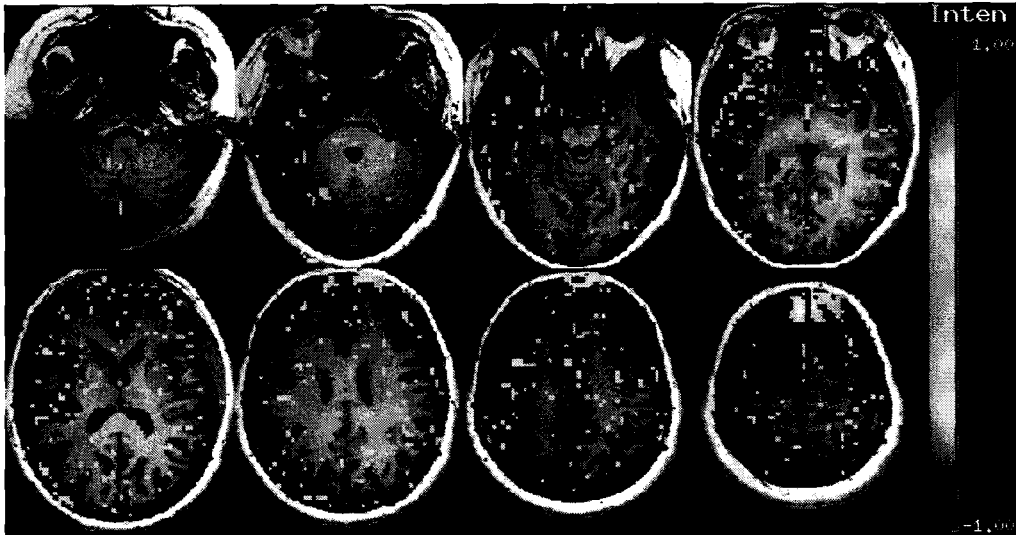


Figure 10.6: The t-score maps (thresholded at t-score = 2.44, $p = 0.0505$) based on the VBM result. Voxel by voxel λ_2 value comparison between the healthy volunteers and CIPN patients was done.

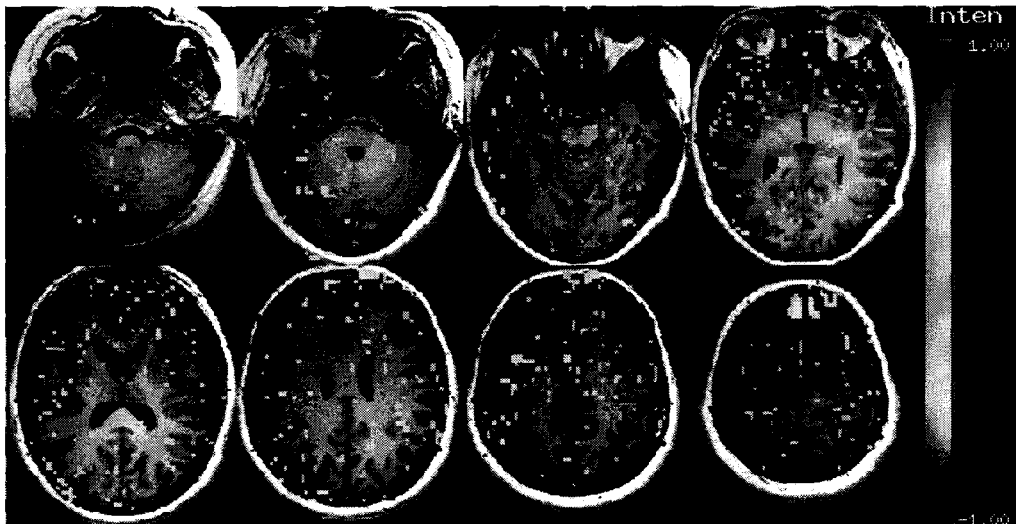


Figure 10.7: The t-score maps (thresholded at t-score = 2.44, $p = 0.0505$) based on the VBM result. Voxel by voxel λ_3 value comparison between the healthy volunteers and CIPN patients was done.

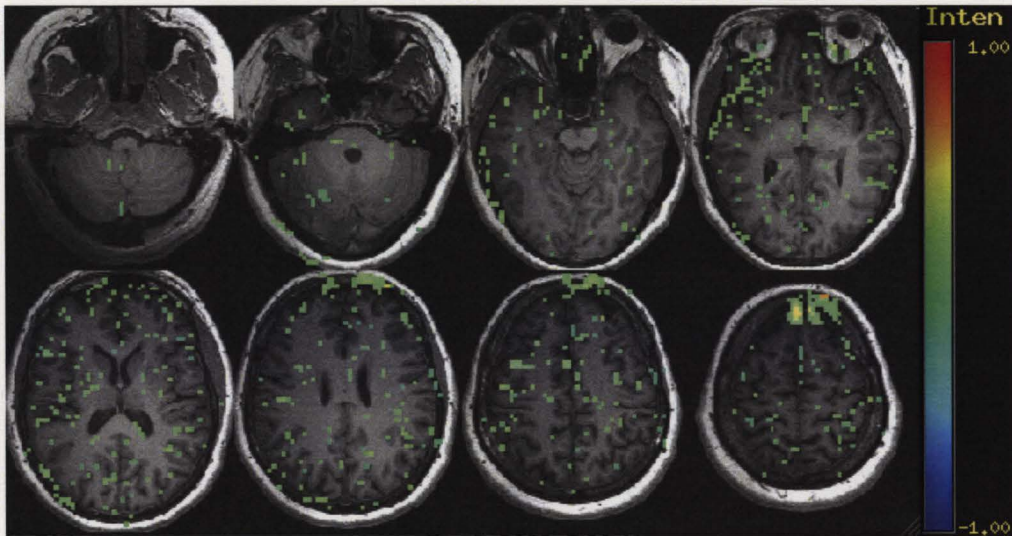


Figure 10.6: The t-score maps (thresholded at $t\text{-score} = 2.44$, $p = 0.0505$) based on the VBM result. Voxel by voxel λ_2 value comparison between the healthy volunteers and CIPN patients was done.

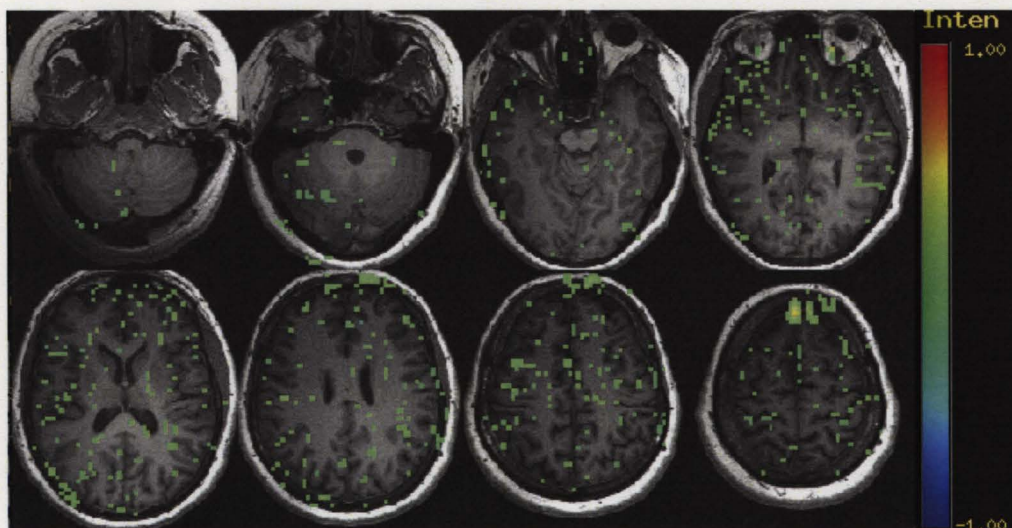
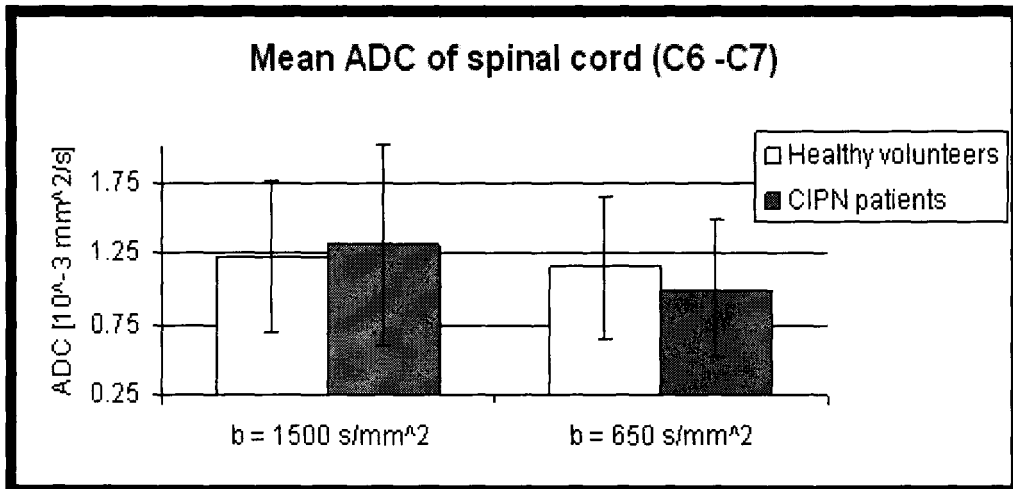
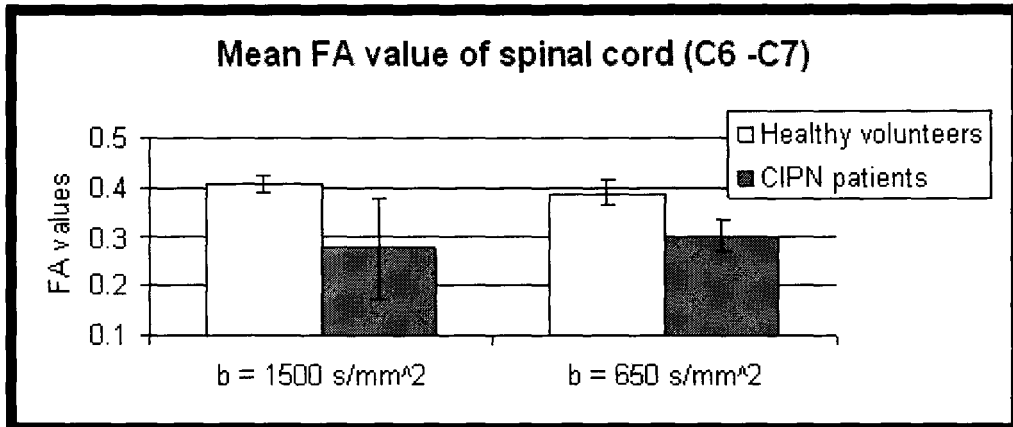
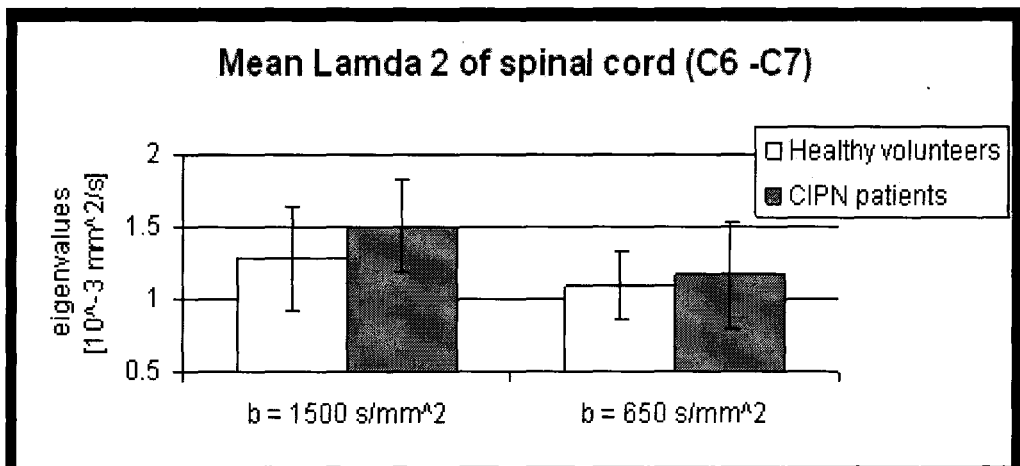
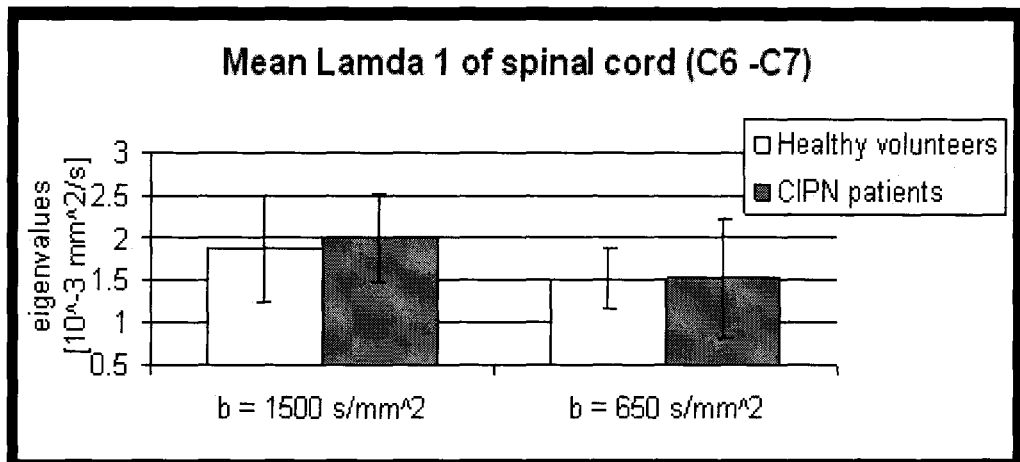


Figure 10.7: The t-score maps (thresholded at $t\text{-score} = 2.44$, $p = 0.0505$) based on the VBM result. Voxel by voxel λ_3 value comparison between the healthy volunteers and CIPN patients was done.

Unlike the brain DTI analysis, VBM analysis was not performed using the spinal cord DTI data. ROI analysis was done on the whole spinal cord. Two sets of spinal cord DTI images are done with b value = 650 s/mm^2 and b value = 1500 s/mm^2 . As discussed in the introduction, there is no clear choice of b-value setting in spinal cord DTI scans. DTI images obtained with low b-value has a higher signal intensity. DTI images obtained with higher b-value, on the other hand, gives diffusion parameter of the water in the microstructures. A t-test was performed to compare the mean FA, mean ADC and mean eigenvalues from the healthy volunteers data (5 subjects, in the age range of 25 to 39 years old) to those from CIPN patients data (3 subjects, in the age range of 50 to 67 years old). Based on results from both b-value data sets, no difference was observed between healthy volunteers and CIPN patients based on ADC and other eigenvalues (refer to Figure 10.8, Table 10.3 and Table 10.4). However, a significantly lowered FA value was evident in CIPN patients when a b-value of 1500 s/mm^2 was applied (t-test = 2.63 > 2.447, 0.05 significant level). In addition, the FA value of the spinal cord for the b= 650 s/mm^2 case seemed to be lower in the CIPN patients than in the healthy volunteers. Although the t-test was 2.17 (< 2.447, 0.05 significant level), the value is s close to the 0.05 significant level (refer to Table 10.3 and

Table 10.4). It is expected that results with higher statistical power may be obtained in the future if more subjects are studied.





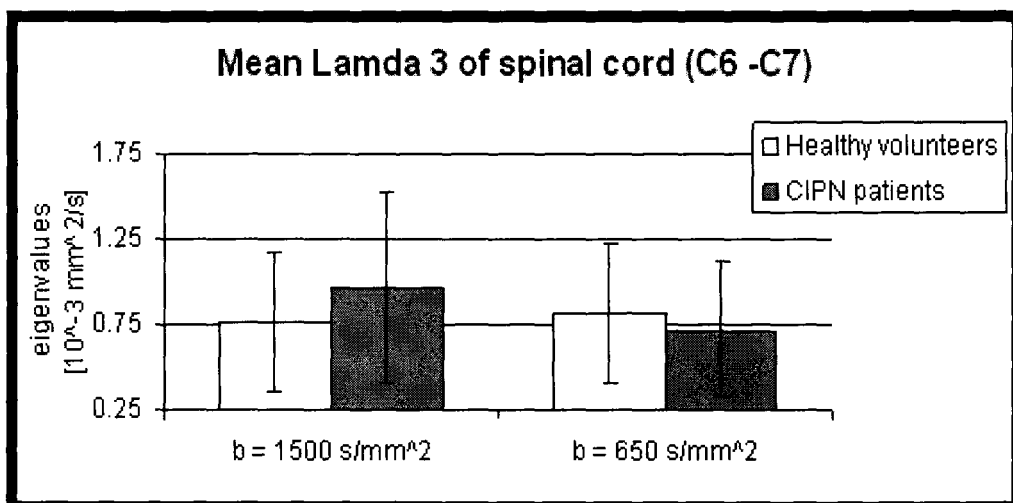


Figure 10.8: The plots of the mean and standard deviation (represented as the error bars) of FA, ADC and eigenvalues (λ_1 , λ_2 and λ_3) using ROI analysis (the whole spinal cord). No difference between the healthy volunteers and the CIPN patients are observed based on the ADC and eigenvalues value of the white matter and grey matter obtained in this study. CIPN patients seem to have a smaller FA value based on the $b=1500\text{s/mm}^2$ case.

	Healthy volunteers		CIPN patients	
	b = 1500 s/mm ²	b = 650 s/mm ²	b = 1500 s/mm ²	b = 650 s/mm ²
FA	0.41±0.02	0.39±0.03	0.28±0.10	0.30±0.03
ADC [$\times 10^3$ mm ² /s]	1.23±0.53	1.16±0.50	1.31±0.71	1.00±0.49
λ_1 [$\times 10^3$ mm ² /s]	1.88±0.63	1.51±0.35	2.00±0.53	1.52±0.72
λ_2 [$\times 10^3$ mm ² /s]	1.28±0.37	1.09±0.24	1.51±0.33	1.16±0.37
λ_3 [$\times 10^3$ mm ² /s]	0.76±0.40	0.782±0.41	0.97±0.56	0.72±0.39

Table 10.3: The result from the spinal cord DTI ROI analysis result. The mean values and the standard deviation of FA, ADC and eigenvalues (λ_1 , λ_2 and λ_3) of each b value settings are determined.

	b=1500 s/mm ²	b=650 s/mm ²
FA	2.63	2.17
ADC [$\times 10^3$ mm ² /s]	0.46	0.05
λ_1 [$\times 10^3$ mm ² /s]	0.28	0.03
λ_2 [$\times 10^3$ mm ² /s]	0.89	0.55
λ_3 [$\times 10^3$ mm ² /s]	0.65	0.66

Table 10.4: t-test result based on the spinal cord DTI result. The mean FA, ADC and eigenvalues from healthy volunteers and CIPN patients are compared. Significant difference is observed in FA value (b=1500 s/mm² case). (p=0.05 level of significant is 2.447)

Direct comparison between the diffusion parameters between the high b-value and low b-value settings (within the same group) was not done. Since the two b-value settings correspond to two different diffusion process, fast diffusion process for low b-value and slow diffusion process for high-value. As indicated in the introduction, high-value setting allows the quantification of

water moving into and out of the microstructure. Low b-value settings gives shorter scan time and shows better SNR, by theory. The effect of those slow diffusion process is being excluded. That is, the tensor calculation is a first-order approximation and the effects of the remaining terms are removed (Mori 2007). When high b-value settings are used, the effect of the fast diffusion process (partially) and some slow diffusion process (mainly) would be included.

10.2 fMRI in the brain

For the purpose to compare the response to temperature, the subjects should be grouped into healthy volunteers, hypersensitive CIPN patients or hyposensitive CIPN patients. The sample size of each categories then becomes: 5 healthy volunteers, 2 hypersensitive CIPN patients and 1 hyposensitive CIPN. Since the number of subjects in the hypersensitive and hyposensitive group was too small, group comparison between the temperature response of these three groups was not done statistically.

Temperature sensation is a graded sensation. It was expected that the BOLD signal would increase as a function of temperature. Voxel-based one factor ANOVA was performed on the healthy volunteers group (5 males) to look for any significant difference between each temperature setting. The

resultant F-stats showed no significant difference in the BOLD signal detected across the temperature settings (Refer to figure 10.9).

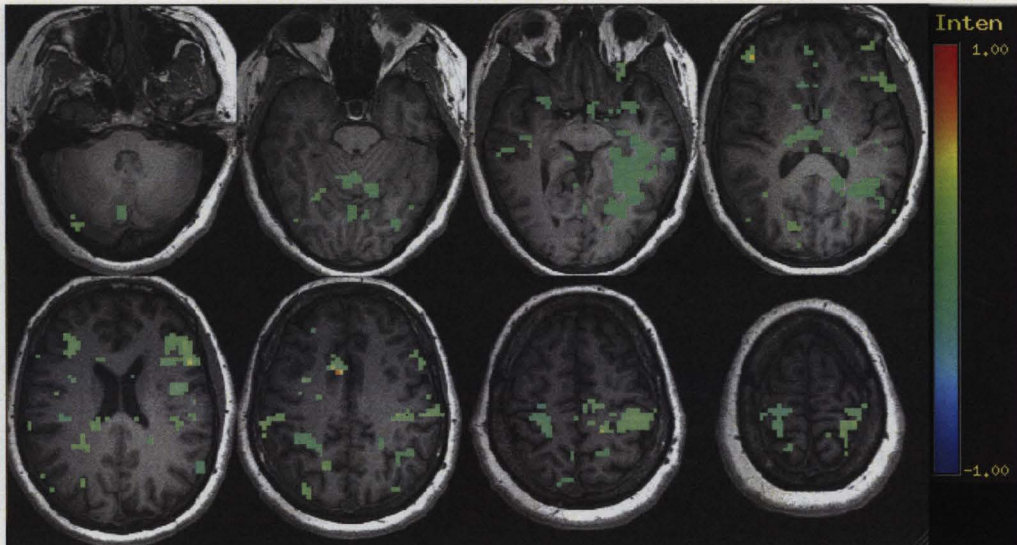


Figure 10.9: The F-map (thresholded at $F = 2.757$, $p = 0.051$) from the ANOVA test based on the result from 5 healthy volunteers. No significant difference between temperature settings is observed. ($F\text{-map} < 5.41$, 0.05 significant level)

The repeated BOLD signal measurements significantly improved the reliability of the fMRI scans. The increment of the temperature settings also ensured that the temperature sensitivity remained strong during each temperature fMRI scan. Multiple regression analysis was performed across the temperature fMRI data of each subject. As shown in figure 10.10, figure 10.11 and figure 10.12, the F-maps generated from multiple regression analysis were sensitive enough to detect the activation.

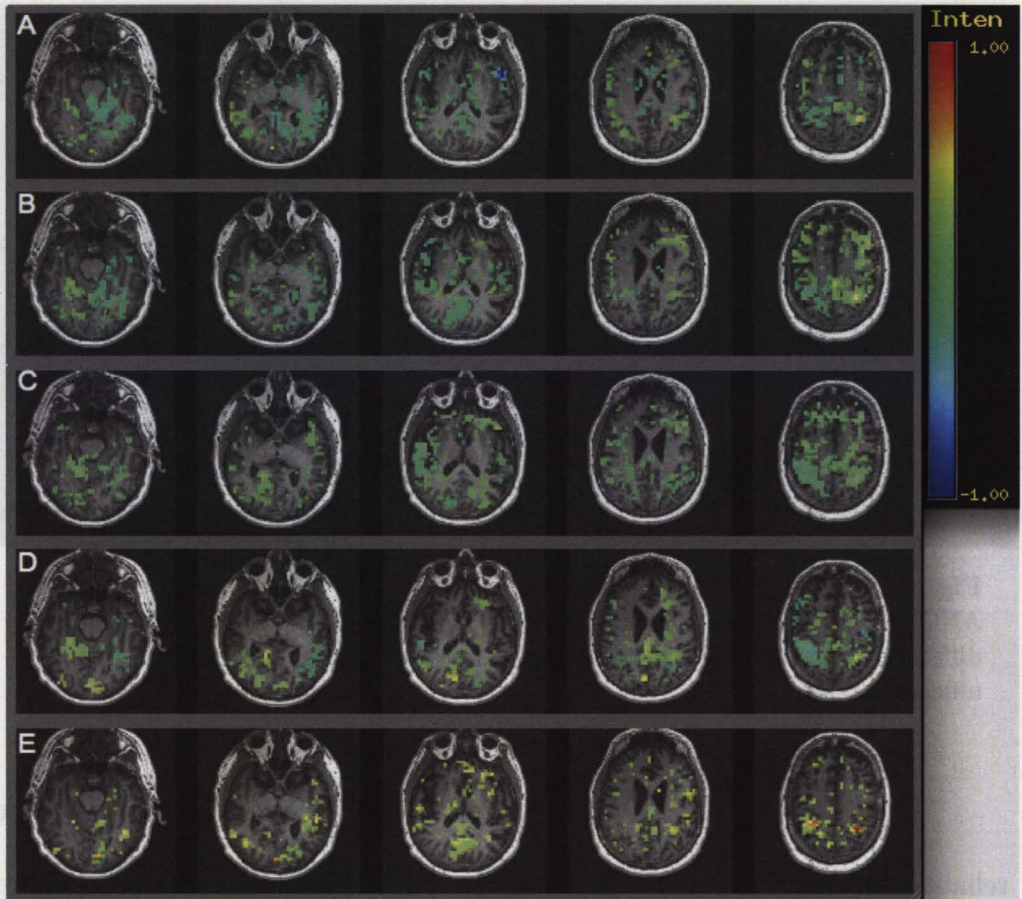


Figure 10.10: Analysis result from the hypersensitive CIPN patient. Figures A to D are the correlation coefficient maps of the same slice (threshold setting: $t=1.98$, $p = 0.0509$) for 12°C , 21°C , 35°C and 40°C , respectively. Activation on the left and right sensory cortex are observed for all temperature settings. Figure E is the F-test map from the multiple regression analysis (threshold setting: $F=5$ $p=6.2 \times 10^{-4}$)

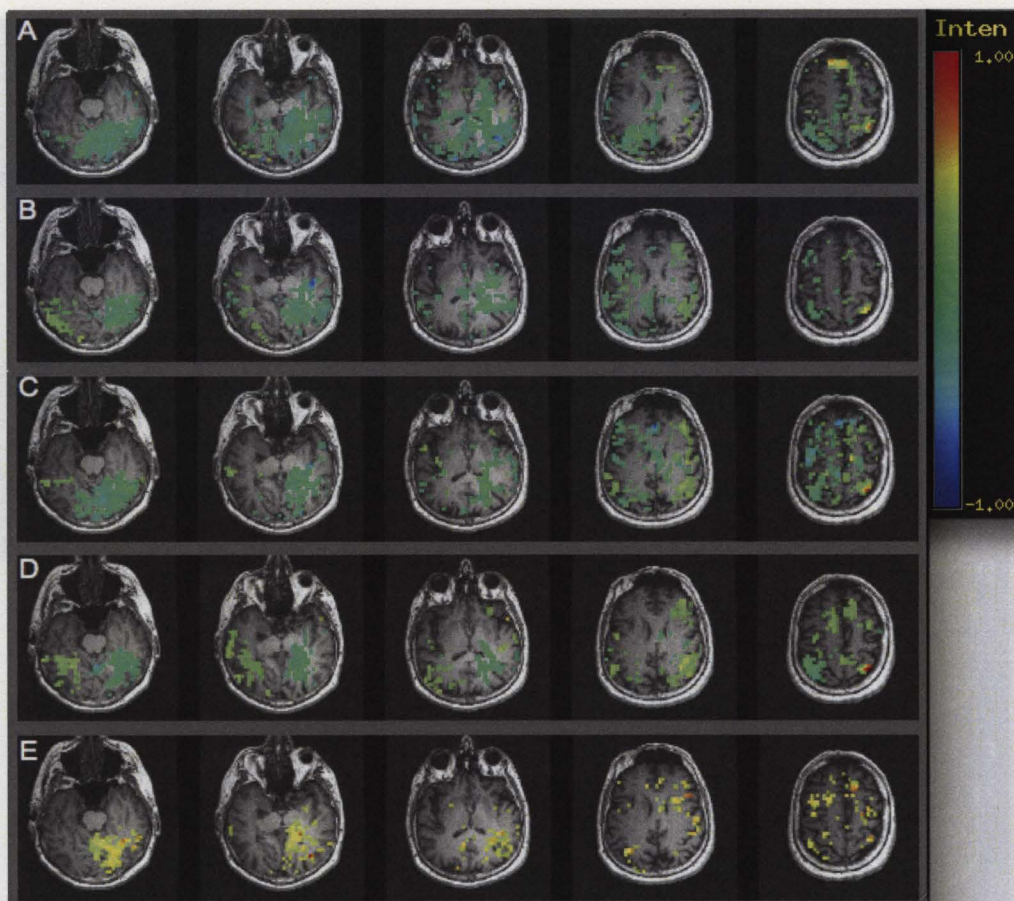


Figure 10.11: Analysis result from the hyposensitive CIPN patient. Figures A to D are the correlation coefficient maps of the same slice (threshold setting: $t=1.98$, $p = 0.0509$) for 12°C , 21°C , 35°C and 40°C , respectively. Activation on the left and right sensory cortex are observed for all temperature settings. Figure E is the F-test map from the multiple regression analysis (threshold setting: $F=5$ $p=6.2 \times 10^{-4}$)

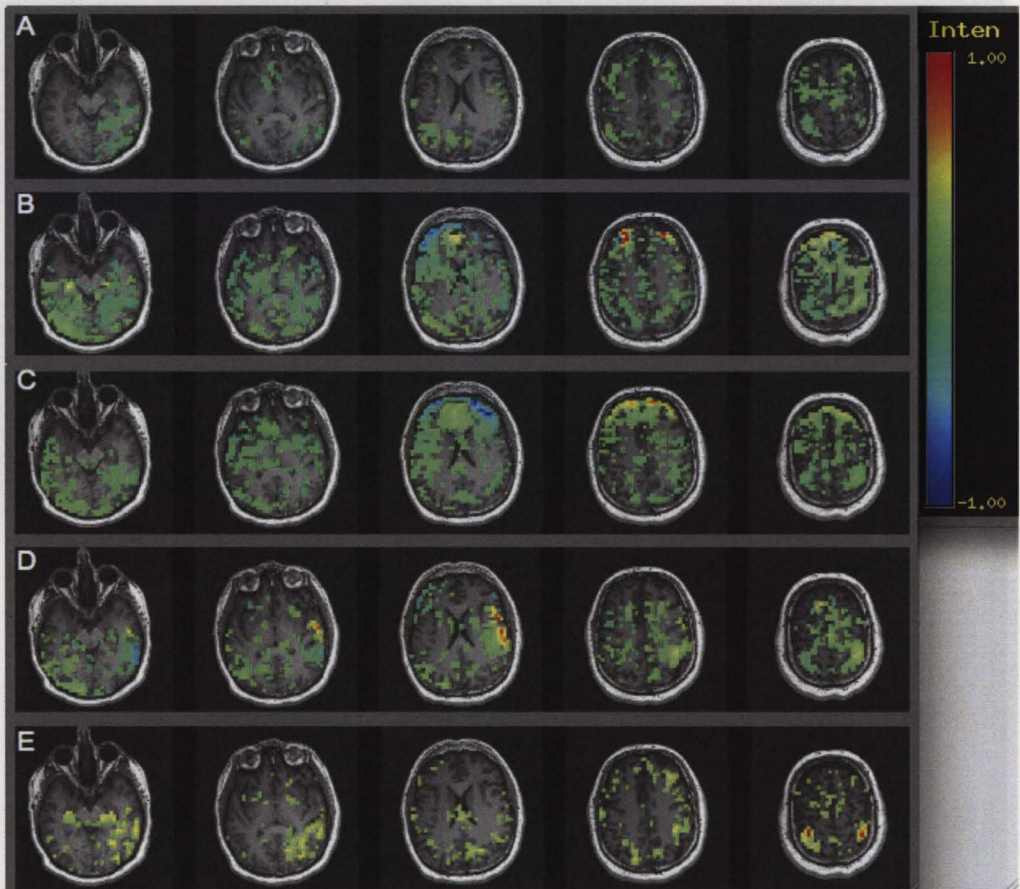


Figure 10.12: Analysis result from a healthy subject. Figures A to D are the correlation coefficient maps of the same slice (threshold setting: $t=1.98$, $p = 0.0509$) for 12°C, 21°C, 35°C and 40°C, respectively. Activation on the left and right sensory cortex are observed for all temperature settings. Figure E is the F-test map from the multiple regression analysis (threshold setting: $F=5$ $p=6.2 \times 10^{-4}$)

As discussed in chapter 2, the side effects of the chemotherapy drugs are usually associated with change in sensory functions. It is thus assumed that the change in the motor cortex (if any) in CIPN patients should be the same. In this case, CIPN patient with elevated temperature sensitivity and those with poor temperature sensitivity will be categorized in the same group. A voxel based t-test was performed to compare the motor fMRI result of healthy control (5 subjects) and that of the CIPN patients (3 subjects). The t-score map was generated based on the finger tapping fMRI scan. As shown in figure 10.13 below, no significant difference was observed between the healthy volunteer group and the CIPN patients. The obtained result agrees with the expectation.

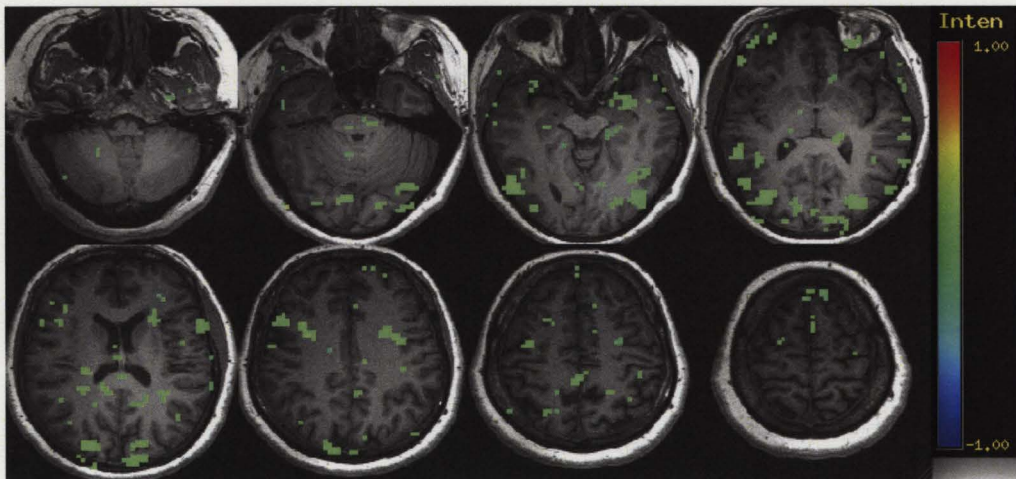


Figure 10.13: The t-score map based on the motor fMRI result. (thresholded at $t=2.510$, $p = 0.0459$). No difference between the healthy volunteer group and the CIPN patients are obtained. This agrees with the expectation that side effects of chemotherapy drugs are usually associated with sensory dysfunction.

As discussed in chapter 2, the side effects of the chemotherapy drugs are usually associated with change in sensory functions. It is thus assumed that the change in the motor cortex (if any) in CIPN patients should be the same. In this case, CIPN patient with elevated temperature sensitivity and those with poor temperature sensitivity will be categorized in the same group. A voxel based t-test was performed to compare the motor fMRI result of healthy control (5 subjects) and that of the CIPN patients (3 subjects). The t-score map was generated based on the finger tapping fMRI scan. As shown in figure 10.13 below, no significant difference was observed between the healthy volunteer group and the CIPN patients. The obtained result agrees with the expectation.

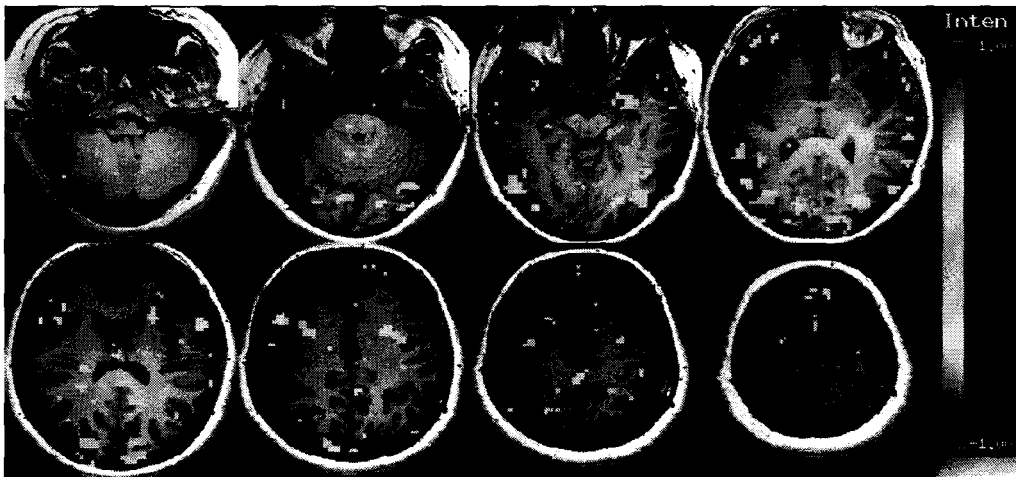


Figure 10.13: The t-score map based on the motor fMRI result. (thresholded at $t=2.510$, $p = 0.0459$). No difference between the healthy volunteer group and the CIPN patients are obtained. This agrees with the expectation that side effects of chemotherapy drugs are usually associated with sensory dysfunction.

Chapter 11

Conclusion and Future directions

Based on the preliminary results of this thesis, only structural changes were observed in the spinal cord. The FA values of the spinal cord (C6 - C7) generated using the high b-value ($b = 1500 \text{ s/mm}^2$) were 0.41 ± 0.02 for the healthy volunteer group and 0.28 ± 0.10 for the CIPN patients. The corresponding FA values generated with the lower b-value ($b = 650 \text{ s/mm}^2$) were 0.39 ± 0.03 for the healthy group and 0.30 ± 0.03 for the CIPN patients. Based on the t-test result, there was a significant decrease in the mean FA value of the CIPN patients when a high b-value was used in the DTI scans. Although the t-test showed no significant difference between the FA value of the CIPN patients and the healthy volunteers (in the low b-value case), the calculated t-score, $t = 2.17$, was close to the $t = 2.447$ (0.05 significant level). Since the sample size was small, the result observed may change as the sample size increases.

If demyelination occurs, the white matter integrity would be reduced. Increases in ADC and eigenvalues; and decrease in FA values in the spinal cord and the brain of CIPN patients are hypothesized. However, not all the

diffusivity parameters follow the predictions. This may be due to the limitation in the small sample size. The difference in the age between the healthy group and the CIPN patient volunteers in this study may have lead to some bias as well.

The spinal cord DTI results also suggested that high b-value setting may give better sensitivity toward structural change of the spinal. DTI scan with high b-values include the slow diffusion component, which may be related to the diffusion process in the microstructures. Some researchers hypothesized that the disturbance of blood vessels may be associated to CIPN. Vascular injury, inflammation and oxidative damaged has been observed and are supporting the hypothesis (Correa and Ahles 2008). The disturbance of the blood vessels may lead to changes in the microscopic structures. In this case, the application of high b-value setting would be superior to the low b-value setting. Since the composition of spinal cord and brain are very similar, the application of high b-value setting in brain DTI scans may be useful in detecting the structural changes in the brain. Sodium imaging of the brain may be another way to look into the structural changes in the brain. As sodium (Na) is one of the important chemical in the neuronal transmission. Any changes in neural response (such as cognitive change and memory) should result in changes in Na concentration. The disturbance of blood vessels would lead to changes in

the level of vasoactivity in the spinal cord and the brain. The measurement of fractal dimension should provide some useful insights into the disease status.

Due to the limitation in the sample size, no statistical comparison between the healthy volunteers and the CIPN patients can be made for the temperature sensitivity fMRI study. However, the multiple regression analysis does give good reliability in detecting the response due to the temperature stimulus. In the motor task fMRI comparison, it was assumed that all CIPN patients had the same motor response in the brain. The corresponding results confirmed the motor function of CIPN patients was comparable to healthy group. This also confirmed that some side effects, such as disorientation, are mainly resulted from the sensory dysfunction.

More CIPN patients will be recruited to complete the temperature sensitivity in the future. Since there is no significant difference between the BOLD response in all four temperature settings, it would be suggested to remove one of the temperature stimulus, 21°C or 35°C, to shorten the total scan time. Although SEEP technique has been applied on the spinal cord and show discouraging results. Since SEEP technique rely on the water movement during neuronal activation, the application of SEEP technique in the brain should provide more information regarding to the brain response.

Bibliography

- Abarham, J., M. Haut, and M. Moran (2008). Adjuvant chemotherapy for breast cancer effects on cerebral white matter seen in diffusion tensor imaging. *Clinical Breast Cancer* 8, 88–91.
- Al-Asmi, A., C.-G. B. ad Don W. Gross, Y. A. Khani, F. Andreemann, B. Pike, F. Dubeau, and J. Gotman (2003). fmri activation in continuous and spike-triggered eeg-fmri studies of epileptic spikes. *Epilepsia* 44, 1328–1399.
- Bammer, R. and F. Fazekas (2003). Diffusion imaging of the human spinal cord and the vertebral column. *Topics in Magnetic Resonance Imaging* 14, 461–476.
- Barker, R. A., M. J. Neal, and S. Barasi (2003). *Neuroscience at a Glance* (Second ed.). Blackwell Publishing Ltd.
- Bihan, D. L., J.-F. Mangin, C. Poupon, C. A. Clark, S. Pappata, N. Molko, and H. Chabriat (2002). Diffusion tensor imaging: concepts and applications. *J Magn Reson Imaging* 13, 534–546.

- Buxton, R. B. (2002). *Introduction to function magnetic resonance imaging: principle and techniques* (First ed.). Cambridge.
- Carpenter, M. B. (1991). *Core test of neuroanatomy* (Fourth ed.). William and Wilkins.
- Clark, C. A. and D. J. Werring (2002). Diffusion tensor imaging in spinal cord: methods and applications - a review. *NMR in Biomedicine* 15, 578-586.
- Correa, D. and T. Ahles (2008). Neurocognitive changes in cancer survivors. *Cancer J* 14, 396-400.
- Custodio, C. M. (2008). Neuromuscular complications of cancer and cancer treatment. *Phys Med Rehabil clin N Am* 19, 27-41.
- Farrell, J. A., S. A. Smith, E. M. Gordon-Lipkin, D. S. Reich, P. A. Calabresi, and P. C. van Zijl (2008). High b-value q-space diffusion-weighted mri of the human cervical spinal cord in vivo: Feasibility and application to multiple sclerosis. *Magn Reson Med* 59, 1079-1089.
- Feng, C.-M., H.-L. Liu, P. T. Fox, and J.-H. Gao (2001). Comparison of the experimental bold signal change in event-related fmri with the balloon model. *NMR in Biomedicine* 14, 397-401.

Figley, C. and P. Stroman (2007). Investigation of human cervical and upper thoracic spinal cord motion: implications for imaging spinal cord structure and function. *Magn Reson Med* 58, 185–189.

Figley, C. and P. Stroman (2009). Development and validation of retrospective spinal cord motion time-course estimates (respice) for spin-echo spinal fmri: Improved sensitivity and specificity by means of a motion-compensating general linear model analysis. *Neuroimage* 44, 421–427.

Forman, A. (1990). Peripheral neuropathy in cancer patients: incidence, features, and pathophysiology. *Oncology (Huntingt)* 4, 57–62.

Gerstl, F., C. Windischbergera, M. Mitterhauserb, W. Wadsakb, A. Holik, K. Kletterb, E. Mosera, S. Kasperc, and R. Lanzenbergerc (2008). Multimodal imaging of human early visual cortex by combining functional and molecular measurements with fmri and pet. *Neuroimage* 41, 204–211.

Greger, R. and U. Windhorst (1996). *Comprehensive human physiology volume 1 From cellular mechanisms to integration*. Springer.

Guyton, A. C. (1991). *Textbook of medical physiology* (Eighth ed.). W.B. Sanuders Company.

- Hashemi, R. H., J. Willian G. Bradley, and C. J. Lisanti (2003). *MRI: the basics* (Second ed.). Lippincott Williams and Wilkins.
- Huettel, S. A., A. W. Song, and G. McCarthy (2003). *Functional magnetic resonance imaging* (First ed.). Sinauer.
- Hwang, S. W. and U. Oh (2007). Current concepts of nociception: nociceptive molecular sensors in sensory neurons. *Current Opinion in Anaesthesiology* 20, 427–434.
- Jin, T., P. Wan, M. Tasker, F. Zhao, and S.-G. Kim (2006). Source of nonlinearity in echo-timedependent bold fmri. *Magn Reson Med* 55, 1281–1290.
- Johnston, M. V. (2009). Plasticity in the developing brain: implications for rehabilitation. *Developmental disabilities research reviews* 15, 94–101.
- Kandel, E. R., james H. Schwartz, and T. M. Jessell (2000). *Principles of neural science* (Forth ed.). McGraw-Hill.
- Liu, H.-L. and J.-H. Gao (2000). An investigation of the impulse functions for the nonlinear bold response in functional mri. *Magn Reson Imaging* 18, 931–938.
- Mabbott, D. J., M. Noseworthy, D. Bouffet, S. Laughlin, and C. Rockel (2006). White matter growth as a mechanism of cognitive development in children. *Neuroimage* 33, 936–946.

- Martini, F. H. (2006). *Fundamentals of anatomy and physiology* (Seventh ed.). Pearson.
- McRobbie, D. W., E. A. More, M. J. Groves, and M. R. Prince (2006). *MRI from picture to proton* (second ed.). Cambridge university press.
- Mori, S. (2007). *Introduction to diffusion tensor imaging* (First ed.). Elsevier.
- Naganawa, S., T. Koshikawa, H. Kawai, H. Fukatsu, T. Ishigak, K. Maruyama, and O. Takizawa (2004). Optimization of diffusion-tensor mr imaging data acquisition parameter for brain fiber tracking using parallel imaging at 3t. *Eur Radiol* 14, 234–238.
- Nishimura, D. G. (1996). *Principles of Magnetic Resonance Imaging*.
- Ogawa, S., T. Lee, A. Kay, and D. Tank (1990). Brain magntic resonance imaging with contrast dependent on blood oxygenation. *Proc. Natl. Acad. Sci* 87, 9868–9872.
- Pfeuffer, J., J. C. McCullough, P.-F. V. de Moortele, K. Ugurbil, and X. Hu (2003). Spatial dependence of the nonlinear bold response at short stimulus duration. *Neuroimage* 18, 990–1000.
- Porto, L., C. Preibisch, E. Hattingen, M. Bartels, T. Lehrnbecher, R. Dewitz, F. Zanella, C. Good, H. Lanfermann, R. DuMesnil, and M. Kieslich

(2008). Voxel-based morphometry and diffusion-tensor mr imaging of the brain in long-term survivors of childhood leukemia. *Eur Radiol.* *18*, 2691–2700.

Quasthoff, S. and H. P. Hartung (2002). Chemotherapy-induced peripheral neuropathy. *J Neuro* *249*, 9–17.

R. Peyron, B. L. and L. Garcia-Larrea (2000). Functional imaging of brain responses to pain. a review and meta-analysis. *Neurophysiol Clin* *30*, 263–288.

Stroman, P., V. Krause, K. Malisza, U. Frankenstein, and B. Tomanek (2002). Extravascular proton density change as a non-bold component of crest in functional mri of the human spinal cord. *MRM* *48*, 122–127.

Stroman, P., A. Lee, K. K. Pitchers, and R. D. Andrew (2008). Magnetic resonance imaging of neuronal and glial swelling as an indication of function in cerebral tissue slices. *MRM* *59*, 700–706.

Stroman, P., B. Tomanek, V. Krause, U. Frankstein, and K. Malisza (2002). Mapping of neuronal function in the healthy and injured human spinal cord with spinal fmri. *NeuroImage* *17*, 1854–1860.

Stroman, P. W. (2005). Magnetic resonance imaging of neuronal function in spinal cord: Spinal fmri. *Clin Med Res.* *3*, 146–156.

Summers, P., P. Staempfli, T. Jaermann, S. Kwiecinski, and S. Kollias (2006). A preliminary study of the effects of trigger timing on diffusion tensor imaging of human spinal cord. *AJNR Am J Neuroradiol* 27, 1952–1961.

Taylor, J. R., C. D. Zafiratos, and M. A. Dubson (2004). *Modern Physics for scientists and engineers* (Second ed.). Pearson Prentice Hall.

Tracey, I., L. Becerra, I. Chang, H. Breiter, L. Jenkins, D. Borsook, and R. G. Gonzalez (2000). Noxious hot and cold stimulation produce common patterns of brain activation in humans: a functional magnetic resonance imaging study. *Neurosci Lett.* 288, 159–162.

Tsuchiya, K., A. Fujikawa, K. Honya, T. Nitatori, and Y. Suzuki (2005). Diffusion tensor tractography of the lower spinal cord. *Neuroradiology* 50, 221–225.

Wickham, R. (2007). Chemotherapy-induced peripheral neuropathy: A review and implications for oncology nursing practice. *Clin J Oncol Nurs.* 11, 361–376.

Zhao, F., M. Willams, X. Meng, D. C. Welsh, A. Colmbra, E. D. Crown, J. J. Cook, M. O. Urban, R. Hargreaves, and D. S. Williams (2008). Bold

and blood volume-weighted fmri of rat lumbar spinal cord non-noxious and noxious electrical hindpaw stimulation. *neuroimage* 40, 133–147.

Zhao, F., M. Williams, X. Meng, D. C. Welsh, I. D. Grachev, R. Hargreaves, and D. S. Williams (2009). Pain fmri in rat cervical spinal cord: an echo planar imaging evaluation of sensitivity of bold and blood volume-weighted fmri. *Neuroimage* 44, 349–362.